Processing of laser altimeter time-of-flight measurements to geodetic coordinates

Haifeng Xiao[1] · Alexander Stark[2] · Gregor Steinbrügge[3] · Hauke Hussmann[2] · Jürgen Oberst[1,2]

Abstract

Laser altimeters are commonly used in planetary research for their high geodetic accuracy. A key procedure in processing of laser altimeter data is the geolocation. In this process, the time-of-flight measurements are converted to coordinates of laser pulse footprints on the surface of the target body. Here, we present a consistent and systematic formulation of three commonly used geolocation models with increasing complexity: static model, spacecraft motion model, pointing aberration model and special relativity model. We show that for small velocities of the spacecraft relative to the target the special relativity model can be reduced to the pointing aberration model without significant loss in the geolocation accuracy. We then discuss the respective accuracies of the proposed models and apply them to time-of-flight measurements from the Mars Orbiter Laser Altimeter (MOLA) onboard the Mars Global Surveyor (MGS) spacecraft and the Mercury Laser Altimeter (MLA) onboard the MErcury Surface, Space ENvironment, GEochemistry and Ranging spacecraft (MESSENGER). While, the archived datasets had not considered the effect of pointing aberration, we demonstrate that a correction due to pointing aberration makes insignificant improvements of 4–5 m laterally and up to ±3 cm radially for MOLA profiles, these figures enormously increase to up to about 150 m laterally and ±25 m radially when applied to the MLA orbital profiles.

Keywords Laser altimetry · Geolocation · MOLA · MLA · Pointing aberration · Special relativity · Mercury · Mars

✉ Haifeng Xiao
  Haifeng.Xiao@campus.tu-berlin.de

  Alexander Stark
  Alexander.Stark@dlr.de

  Gregor Steinbrügge
  gbs@stanford.edu

  Hauke Hussmann
  Hauke.Hussmann@dlr.de

  Jürgen Oberst
  Juergen.Oberst@dlr.de

[1] Institute of Geodesy and Geoinformation Science, Technische Universität Berlin, Berlin, Germany

[2] Institute of Planetary Research, German Aerospace Center (DLR), Berlin, Germany

[3] Department of Geophysics, Stanford University, Stanford, USA

1 Introduction

A laser altimeter is an instrument aiming at a precise measurement of distances. The high precision is obtained by accurate measurement of the time-of-flight (ToF) of short (few ns) laser pulses. A laser footprint is the spot area illuminated by a single laser pulse, which varies with the laser beam divergence angle, the ranging geometry and the encountered terrain. In planetary exploration, these instruments are very useful for the derivation of shape and topography of a celestial object (e.g., Perry et al. 2015). By studying the reflected laser pulse from the surface, it is possible to derive surface albedo and roughness at footprint scale (Smith et al. 2001a; Neumann et al. 2016; Smith et al. 2017). Furthermore, differential range measurements at intersecting profiles (cross-over points) can be used for tidal deformation measurements (Mazarico et al. 2014a; Steinbrügge et al. 2015, 2018) and for precise orbit determination (e.g., Rowlands et al. 1999; Mazarico et al. 2010). Co-registration of laser altimeter data with topography information derived from stereo images can be used for rotation measurements (Stark et al. 2015) and to

improve the spatial coverage of the merged product (Barker et al. 2016).

Due to their high measurement accuracy, laser altimeters continue to be used in planetary exploration (Hussmann 2014; Hussmann et al. 2019). Most recently, we have seen launches of the BepiColombo Laser Altimeter (BELA) (Thomas et al. 2007, 2019) onboard the Mercury Planetary Orbiter (MPO), the OSIRIS-REx Laser Altimeter (OLA) (Daly et al. 2017) onboard the Origins Spectral Interpretation Resource Identification Security-Regolith Explorer (OSIRIS-REx) and the LIght Detection And Ranging (LIDAR) onboard Hayabusa2 (Mizuno et al. 2017).

The concept of the laser altimetry is to measure the round-trip ToF of laser pulses emitted to the surface and reflected back at the instrument's receiver. Currently, four commonly adopted methods to measure the ToF exist: leading edge detection, waveform processing and analyzing, constant fraction discrimination and photon counting (see Zhou et al. 2017, for details). The ToF measurement itself is typically performed with an ultra stable oscillator (USO) featuring a high frequency stability over short time intervals (μs). Typically, the long-term drift and aging of the laser altimeter USO is such that it requires recurrent calibration using the spacecraft's clock (Abshire et al. 2000; Sun and Neumann 2015). The laser altimeter USO is calibrated against the spacecraft clock which is monitored and calibrated using radio links to Earth. As a consequence, the ToF measurements are expressed in Barycentric Dynamical Time (TDB) scale, instead of the proper time of the spacecraft. The implication of this is presented in Sect. 2.4, and the conversion of these two timescales is detailed Section A in Appendices. The measured ToF might require additional calibration due to broadened return pulses (range walk) and delays in the receiver electronics (Abshire et al. 2000; Sun and Neumann 2015). Typically, the measured ToF is downlinked to Earth and associated with a surface coordinate using auxiliary information from the spacecraft (trajectory and pointing). The purpose of the here presented paper is to discusses this critical processing step, the *geolocation*, and to reveal important differences in the derived surface coordinates depending on underlying assumptions. For the Mars Orbiter Laser Altimeter (MOLA) onboard the Mars Global Surveyor (MGS) spacecraft and the Mercury Laser Altimeter (MLA) onboard the MErcury Surface, Space ENvironment, GEochemistry and Ranging (MESSENGER) spacecraft, there have been some brief descriptions of their geolocation processes in user guide documents as distributed with the corresponding data products in the Planetary Data System (PDS) Geosciences Node (Smith et al. 2003b; Neumann 2016). The difference in the positions of the spacecraft at laser transmission and reception has been considered. There are detailed geolocation specifications for some precise laser altimeters for applications on Earth, e.g., the Ice, Cloud and Land Elevation Satellite (ICESat) Geoscience Laser Altimeter System (GLAS) (Shutz and Urban 2014), recently deployed ICESat-2 Advanced Topographic Laser Altimeter System (ATLAS) (Luthcke et al. 2019a) and the Global Ecosystem Dynamics Investigation (GEDI) laser ranging system (Luthcke et al. 2019b). The ICESat missions are designed mainly for high-precision measurement of height change of Earth's cryosphere, e.g., Antarctic and Greenland ice sheets and high-altitude mountain glaciers; thus, any factor that might affect the geolocation will need to be examined and taken care of. Indeed, both the spacecraft's motion during ToF and pointing aberration have been incorporated into their geolocation models. In this paper, we will give a consistent and systematic formulation of three geolocation models: static model (SM), spacecraft motion model (SMM) and pointing aberration model (PAM). For the two most typically used models, i.e., SMM and PAM, we will additionally introduce in the concept of the external observer which could be any body including the spacecraft itself. In addition, we will present the novel special relativity model (SRM) which copes with the special relativity effects due to the relative velocity of the spacecraft with respect to the target body. Furthermore, it will be shown that the pointing aberration correction for PAM could be directly deduced from SRM under some assumptions. Using the cases of MOLA and MLA, it will also be shown that for a spacecraft on an elliptic orbit the effect of pointing aberration, caused by the relative velocity of the spacecraft with respect to the observer, can lead to significant lateral and vertical displacement of the footprint coordinates. It is worth noting that none of the geolocation models presented here have dealt with the inherent orbit, pointing and timing errors which could significantly degrade the geolocation process. Thus, additional calibrations to eliminate these error types are needed to further improve the geolocation accuracy, e.g., terrain matching, ground-based laser detector approach, cross-over analysis, satellite commanded maneuver method and so on (Rowlands et al. 1999; Neumann et al. 2001; Luthcke et al. 2005; Magruder et al. 2005). In particular, the accuracy of planetary laser altimetry is often limited by significantly larger unmodeled orbit, attitude errors and less precise transformation from inertial to planet body-fixed coordinates than in the terrestrial case.

The paper is structured as follows: In Sect. 2, four geolocation models designed to convert the ToF measurements to footprint geodetic coordinates will be introduced. This will be followed by applications of these models to MOLA and to MLA in Sects. 3 and 4, respectively. Discussions of the MOLA and MLA results and their implications are presented in Sect. 5, and finally, conclusions are drawn in Sect. 6.

2 Geolocation in laser altimetry

The process of geolocation, i.e., the conversion of ToF measurements to surface coordinates in the body-fixed reference frame of the target body, can be divided into two steps. In the first step, the ToF measurements are combined with instrument orientation, spacecraft orbit position and pointing to retrieve coordinates of the footprints in the International Celestial Reference Frame (ICRF) centered at the center of mass (CoM) of the target body. For the computation of the inertial coordinates r_{in}, we will systematically formulate three commonly used geolocation models (SM, SMM and PAM) with increasing complexity and accuracy. Then, we will present the fourth model, i.e., SRM, to account for the effects of special relativity and examine its relation to PAM. Before we discuss these models, we outline the second step which consists of the transformation of the inertial coordinates to body-fixed coordinates by evaluating an appropriate rotation model for the target body at the time of the laser pulse reflection. With r_{in} denoting the inertial coordinates of the footprint with respect to the CoM of the target body, the body-fixed coordinates can be obtained by

$$r_{bf} = R_{in \to bf}(t^*) \cdot r_{in}, \tag{1}$$

where r_{bf} are the body-fixed coordinates and t^* is the time of the reflection in TDB timescale. The transformation matrix $R_{in \to bf}$ can be expressed as

$$R_{in \to bf} = R_z\left(W(t^*)\right) R_x\left(\frac{\pi}{2} - \delta(t^*)\right) R_z\left(\frac{\pi}{2} + \alpha(t^*)\right), \tag{2}$$

with the time-dependent Euler angles α, δ and W denoting the right ascension, declination and prime meridian angle, respectively (see Archinal et al. 2018, for details). $R_{x,z}$ denotes counterclockwise rotation matrices about the respective axis

$$R_x(\theta) = \begin{bmatrix} 1 & 0 & 0 \\ 0 & \cos\theta & -\sin\theta \\ 0 & \sin\theta & \cos\theta \end{bmatrix}$$

$$R_z(\theta) = \begin{bmatrix} \cos\theta & -\sin\theta & 0 \\ \sin\theta & \cos\theta & 0 \\ 0 & 0 & 1 \end{bmatrix}. \tag{3}$$

2.1 Static model

We start with the *static model* (SM) which is the simplest among the proposed models. It basically corresponds to the case where the speed of the spacecraft and hence its relative motion during ToF are ignored. It is equivalent to the case in which the speed of light is assumed to reach infinity. Under
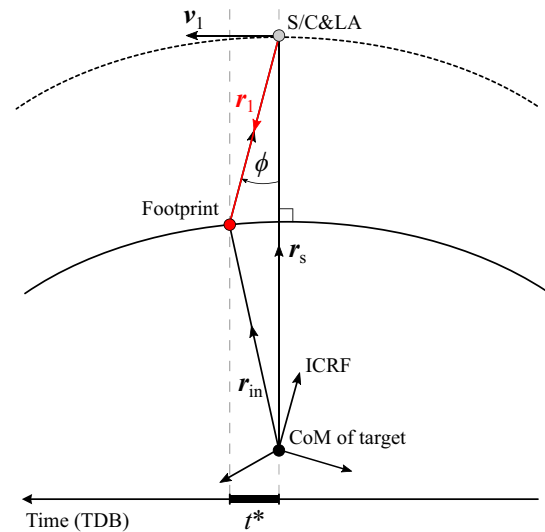

Fig. 1 Scheme for the laser altimeter measurement within the static model (SM). r_{in} is the position vector of the footprint, r_1 is the laser pulse one-way transmit vector, r_s is the position vector of the spacecraft, v_1 is the velocity vector of the spacecraft relative to the target body, and ϕ is the off-nadir angle of the emitted laser beam. All vectors are evaluated at time t^* and refer to the ICRF centered at the CoM of the target body

this assumption, the emission, reflection and detection of the laser pulse are then condensed to a concurrent event at t^* (Fig. 1). With these approximations, the derivation of the inertial coordinates r_{in} is straightforward. The laser pulse one-way transmit vector r_1 (Fig. 1) is obtained by an equation often cited in connection to laser altimetry

$$r_1 = \frac{c\tau}{2} e_1, \tag{4}$$

where c is the speed of light in vacuum, τ is the ToF and e_1 is the normalized boresight vector denoting the orientation of the emitter of the laser altimeter. With r_1 given, the inertial coordinates of the footprint are obtained by

$$r_{in} = r_s + r_1, \tag{5}$$

with r_s being the positional vector of the spacecraft with respect to the target's CoM. The local radius of the target body at the footprint location $r_{in} = |r_{in}|$ can be expressed as

$$r_{in} = \sqrt{r_s^2 + r_1^2 - 2 r_s \cdot r_1} \tag{6}$$

$$= \sqrt{r_s^2 + r_1^2 - 2 r_s r_1 \cos\phi}, \tag{7}$$

where $r_s = |r_s|$ is the distance from CoM to the spacecraft, $r_1 = |r_1|$ is the one-way range and ϕ is the off-nadir angle. Note that Eq. (7) is identical to Eq. (2) in Abshire et al. (2000).
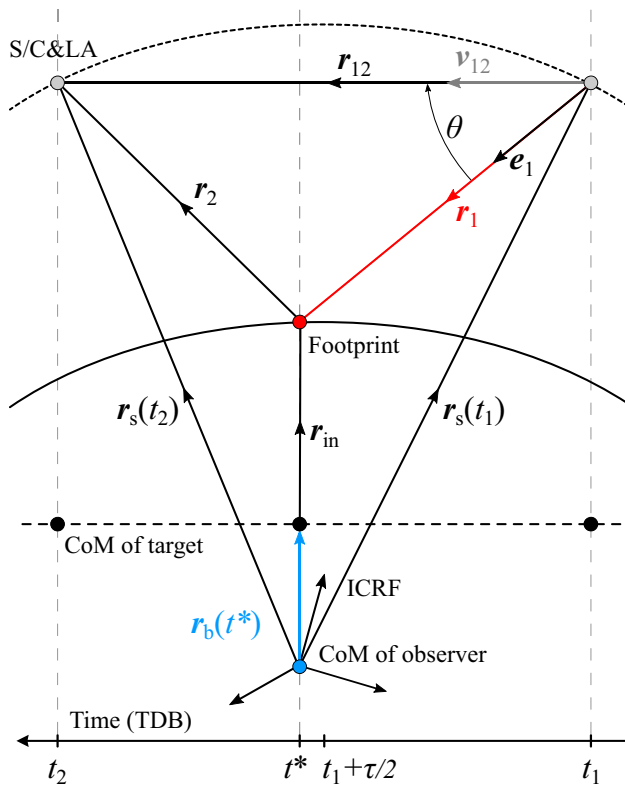
Fig. 2 Scheme of the spacecraft motion model (SMM). r_{in} is the positional vector of the bounce point with respect to the target body. r_1 is the one-way vector of the outgoing leg, while r_2 is the receipt leg. r_{12} is the vector directed from the spacecraft's position at t_1 to that at $t_2 = t_1 + \tau$. The $r_s(t_1)$ and $r_s(t_2)$ are the spacecraft's position vectors with respect to the CoM of the observer at t_1 and t_2, respectively. $r_b(t^*)$ is the position vector of the CoM of the target body with respect to the CoM of the observer at the reflection time t^*

2.2 Spacecraft motion model

In the second model, we now account for the spacecraft's motion between the transmission and reception of the laser pulse. The geometry for the spacecraft motion model (SMM) is shown in Fig. 2. To enable for different observers, we have generalized the observation conditions with an external observer which could be any body in the Solar System including the spacecraft itself. Here, the measured quantities are the laser transmission time stamp t_1 and receipt time stamp t_2 (hence the ToF $\tau = t_2 - t_1$), while the unknown to be solved is the footprint positional vector with respect to the CoM of target body r_{in} at the reflection time t^*. It can be vividly imaged that a string of length of the two-way range is attached at the ends to the spacecraft evaluated at laser transmission $r_s(t_1)$ and reception $r_s(t_2)$. The string is pulled along the laser boresight e_1 until it is tight and the point at which it becomes tight is the bounce point. As in the previous model, the position vectors of the spacecraft at pulse transmission $r_s(t_1)$, at pulse reception $r_s(t_2)$ and the location

of the target body $r_b(t^*)$ can be readily known as long as the required spacecraft and planetary ephemerides are provided. With these vectors, the change in spacecraft position during the ToF is obtained through

$$r_{12} = r_s(t_2) - r_s(t_1). \tag{8}$$

Given that r_{12} is known from spacecraft ephemeris, the angle θ between r_{12} and the boresight normalized vector $e_1 = e_{la}(t_1)$ at time t_1 can be computed by

$$\cos\theta = \frac{r_{12} \cdot e_1}{r_{12}} = \frac{v_{12} \cdot e_1}{v_{12}}. \tag{9}$$

Considering the triangle formed by r_1, r_2 and r_{12}, and applying the Law of Cosines, one obtains

$$r_1^2 + r_{12}^2 - r_2^2 = 2r_1 r_{12} \cos\theta = 2r_1 r_{12} \cdot e_1. \tag{10}$$

Another constraint is that the sum of the norms of r_1 and r_2 corresponding to two sides of the triangle in question equals the total distance the laser pulse has traveled, and is the two-way range $c\tau$:

$$r_1 + r_2 = c\tau. \tag{11}$$

Combining Eqs. (8)–(11), the geometric solution of the norm of the emission leg r_1 is

$$r_1 = \frac{r_{12}^2 - c^2\tau^2}{2(r_{12} \cdot e_1 - c\tau)} = \frac{c\tau}{2} \frac{(r_{12}/c\tau)^2 - 1}{r_{12}/c\tau \cdot e_1 - 1}. \tag{12}$$

Considering that $r_{12}/\tau = v_{12}$ and using $\boldsymbol{\beta} = (\beta_x, \beta_y, \beta_z)^{\mathrm{T}} = v_{12}/c$, we can write

$$r_1 = \frac{c\tau}{2} \frac{\beta^2 - 1}{\boldsymbol{\beta} \cdot e_1 - 1} = \frac{c\tau}{2} - \delta, \tag{13}$$

with $\beta = |\boldsymbol{\beta}|$ and the range difference δ given by

$$\delta = \frac{c\tau}{2} \frac{\boldsymbol{\beta} \cdot e_1 - \beta^2}{\boldsymbol{\beta} \cdot e_1 - 1}$$
$$= \frac{c\tau}{2} \left(-\beta\cos\theta + \beta^2\sin^2\theta\right) + \mathcal{O}(\beta^3). \tag{14}$$

Following this derivation, the laser pulse is reflected at the surface at

$$t^* = t_1 + \frac{r_1}{c} = t_1 + \frac{\tau}{2} \frac{\beta^2 - 1}{\boldsymbol{\beta} \cdot e_1 - 1}$$
$$= t_1 + \frac{\tau}{2}(1 + \beta\cos\theta) + \mathcal{O}(\beta^2). \tag{15}$$

When $\theta \leq 90°$, then $\beta\cos\theta \geq 0$, the time of reflection is thus always longer than or equals a half of ToF $t^* - t_1 \geq \tau/2$

and the outgoing leg is longer than or equals the receipt leg $r_1 \geq r_2$.

Finally, the position vector of the bounce point with respect to the CoM of the target body is given by

$$
\begin{aligned}
\boldsymbol{r}_{\mathrm{in}} &= r_1 \boldsymbol{e}_1 + \boldsymbol{r}_{\mathrm{s}}(t_1) - \boldsymbol{r}_{\mathrm{b}}(t^*) \\
&= \frac{c\tau}{2} \frac{\beta^2 - 1}{\boldsymbol{\beta} \cdot \boldsymbol{e}_1 - 1} \boldsymbol{e}_1 + \boldsymbol{r}_{\mathrm{s}}(t_1) - \boldsymbol{r}_{\mathrm{b}}(t^*).
\end{aligned} \tag{16}
$$

For small β, we may write

$$
\boldsymbol{r}_{\mathrm{in}} = \frac{c\tau}{2} \boldsymbol{e}_1 (1 + \beta \cos\theta) + \boldsymbol{r}_{\mathrm{s}}(t_1) - \boldsymbol{r}_{\mathrm{b}}(t^*) + \mathcal{O}(\beta^2). \tag{17}
$$

If the CoM of the target body is assumed as the observer, i.e., $\boldsymbol{r}_{\mathrm{b}}(t^*) = 0$, and if we assume that $r_{12} \ll c\tau$ ($\beta \approx 0$), Eq. (16) is equivalent to the expression of the static model described in Sect. 2.1. Typically, β is about 10^{-5} for spacecraft in planetary orbits or when performing flybys. Such small values for β might be considered negligible, but can lead to range differences δ as large as 10 m when ranging in the direction of the target body ($\theta = 0$) from a distance of 1000 km. Critical for the effect is the product $\boldsymbol{\beta} \cdot \boldsymbol{e}_1 = \beta \cos\theta$, i.e., the direction of the pulse emission with respect to the spacecraft's direction of motion. The more the two directions coincide ($\theta \approx 0 \rightarrow \beta \cos\theta \approx \beta$), i.e., the higher the off-nadir angle and/or the higher the orbital eccentricity, the larger becomes the absolute values of δ. For range measurements performed from a circular orbit with nadir pointing, i.e., $\theta = 90°$, the range difference δ is typically below 1 mm and the result is comparable to the static model. These findings will be confirmed when applying the geolocation methods to MLA data (large off-nadir angles on an eccentric orbit) in Sect. 4.

2.3 Pointing aberration model

An important aspect of the geolocation process is the dependence of $\boldsymbol{e}_1$ on the relative velocity of the spacecraft with respect to the observer. This effect is known as *aberration* and can be of significant importance for both the lateral and radial positions of the laser pulse footprint. Typically, the orientation of the spacecraft (and consequently of the laser altimeter transmitter) is expressed with respect to a reference frame centered at the spacecraft. This implies that in case another observer than the spacecraft is chosen, Eq. (16) is only correct when the emission direction $\boldsymbol{e}_1$ is corrected for aberration. We will therefore present the pointing aberration model (PAM) which features an observer-independent treatment. The geometry of this model is depicted in Fig. 3. The pointing aberration model is an extension of the spacecraft motion model and differs from it only in that it takes the pointing aberration into account. By applying the velocity
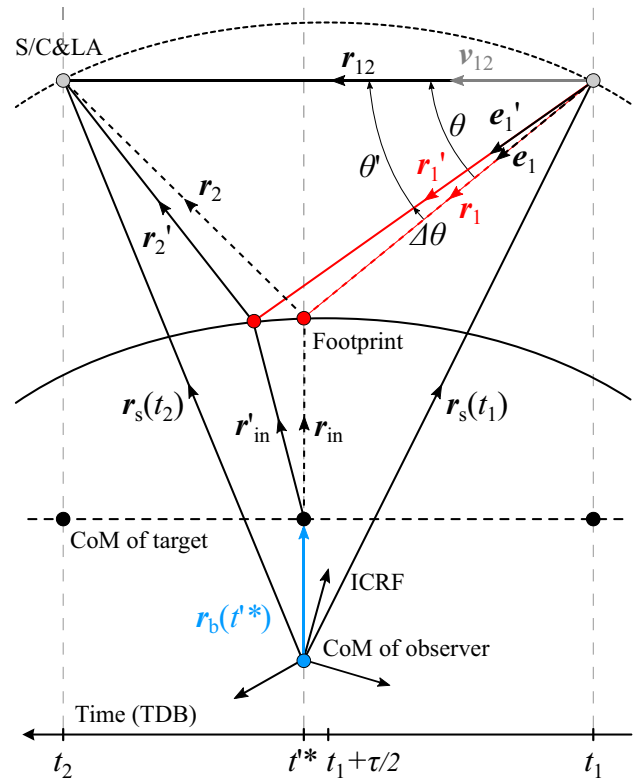

Fig. 3 Scheme of the pointing aberration model (PAM). The same nomenclature is applied as shown in Fig. 2. The aberration correction angle is denoted by $\Delta\theta$

aberration correction to the initial boresight unit vector $\boldsymbol{e}_1$ to account for the relative velocity of the spacecraft with respect to the observer, we obtain the corrected boresight unit vector $\boldsymbol{e}_1'$ that defines the one-way vector $\boldsymbol{r}_1'$ in Fig. 3. The corrected boresight vector $\boldsymbol{e}_1'$ can be obtained by the parallelogram law of addition of velocity vectors $\boldsymbol{v}_{12}$ and $c\boldsymbol{e}_1$

$$
\boldsymbol{e}_1' = \frac{\boldsymbol{v}_{12} + c\boldsymbol{e}_1}{|\boldsymbol{v}_{12} + c\boldsymbol{e}_1|} = \frac{\boldsymbol{e}_1 + \boldsymbol{\beta}}{\sqrt{\beta^2 + 2\boldsymbol{\beta} \cdot \boldsymbol{e}_1 + 1}}. \tag{18}
$$

Note that Eq. (18) is a nonrelativistic approach which manifests itself in an absolute velocity that can become greater than the speed of light if the boresight vector $\boldsymbol{e}_1$ has a component parallel to $\boldsymbol{v}_{12}$. However, we find that in practice this approximation works reasonably well (Bae and Schutz 2002; Luthcke et al. 2019a, b). A fully relativistic approach will be presented in Sect. 2.4.

The magnitude of the pointing aberration depends on the component of the relative velocity of the spacecraft and the observer $\boldsymbol{v}_{12}$ that is perpendicular to the laser altimeter initial

boresight e_1 (Bae and Schutz 2002)

$$\Delta\theta = \arccos\left(e_1 \cdot e_1'\right)$$

$$= \arccos\left(\frac{\beta\cos\theta + 1}{\sqrt{\beta^2 + 2\beta\cos\theta + 1}}\right) \tag{19}$$

$$= \beta\sin\theta + \mathcal{O}\left(\beta^2\right) \approx \frac{v_{12}}{c}\sin\theta,$$

where θ represents the angular separation between v_{12} and the laser altimeter's uncorrected boresight unit vector e_1, i.e., $\cos\theta = \boldsymbol{\beta} \cdot e_1/\beta$. As can be observed from Eq. (19), the aberration correction $\Delta\theta$ increases with the relative velocity v_{12}, but is minimized for pulse emissions in flight direction, i.e., $\theta \approx 0$.

Using the corrected boresight vector, the one-way vector becomes

$$r_1' = r_1'e_1' = \frac{c\tau}{2}\frac{\beta^2 - 1}{\boldsymbol{\beta}\cdot e_1' - 1}e_1'$$

$$= \frac{c\tau}{2}\frac{\beta^2 - 1}{\beta^2 + \boldsymbol{\beta}\cdot e_1 - \sqrt{\beta^2 + 2\boldsymbol{\beta}\cdot e_1 + 1}}\left(e_1 + \boldsymbol{\beta}\right). \tag{20}$$

Analogous to Sect. 2.2, the time at which the laser pulse is reflected by the surface is given by $t'^* = t_1 + r_1'/c$ and the position vector of the bounce point with respect to the CoM of the target body becomes

$$r_{\text{in}}' = r_1' + r_s(t_1) - r_b(t'^*). \tag{21}$$

In contrast to SMM in which pointing aberration has been neglected, the obtained expression can now be used to obtain consistent and accurate results for all different observers. However, for applications concerned with high accuracy of footprint coordinates, such as cross-over analysis, a relativistic approach should be considered.

For small relative velocities $\beta \ll 1$, the expression in Eq. (20) can be simplified to

$$r_1' = \frac{c\tau}{2}(e_1 + \boldsymbol{\beta})\left(1 - \frac{1}{2}\beta^2\sin^2\theta\right) + \mathcal{O}(\beta^3), \tag{22}$$

and the one-way range r_1' can be expressed as

$$r_1' = \frac{c\tau}{2} - \delta = \frac{c\tau}{2} + \frac{c\tau}{2}\left(\beta\cos\theta - \frac{1}{2}\beta^3\cos\theta\sin^2\theta\right)$$

$$+ \mathcal{O}(\beta^4). \tag{23}$$

Finally, the footprint coordinates can be written as

$$r_{\text{in}}' = \frac{c\tau}{2}(e_1 + \boldsymbol{\beta})\left(1 - \frac{1}{2}\beta^2\sin^2\theta\right) + r_s(t_1)$$

$$- r_b(t'^*) + \mathcal{O}(\beta^3). \tag{24}$$

The comparison of the derived expression for r_{in}' to the one obtained in SMM reveals that the boresight vector e_1 is now corrected for aberration indicated by the term $e_1 + \boldsymbol{\beta}$. If the spacecraft itself was chosen to be the observer, i.e., $\beta = 0$, then Eq. (24) can be reduced to Eq. (17) in SMM.

2.4 Special relativity model

In the special relativity model (SRM), the observables will be transformed from a quasi-inertial spacecraft-centered ICRF to one centered at the CoM of the target body, accounting for the effects of special relativity. The geometry of the special relativity model is shown in Fig. 4. Two assumptions are made to facilitate this process: (1) The relative velocity of spacecraft and target body v_{12} remains constant between transmission and reception of the laser beam and (2) no effects of general relativity are incorporated.

It is worth mentioning, under the aforementioned assumptions, from the spacecraft's perspective the laser pulse has been fired at t_1, hit the ground at exactly $t_1 + \tau/2$ and then returned at t_2. This means that the reflection of the laser pulse always takes place at the mid of the round-trip ToF. The directions of the laser pulse's outgoing and receipt legs always align with the initial boresight e_1 measured at time tag t_1. However, for an observer located elsewhere, e.g., at the CoM of the target body, the duration and direction of the outgoing and receipt legs might be observed as different.

We consider two four-vectors with origin at t_1 in the Minkowski space referenced to the spacecraft (left panel of Fig. 4). The first four-vector connects the events when the laser pulse leaves the laser altimeter transmitter at t_1 and gets reflected from the target body surface at $t_1 + \tau/2$

$$\mathbf{r}_1 = \begin{bmatrix} c\tau/2 \\ r_1 \end{bmatrix} = \frac{c\tau}{2}\mathbf{e}_1 = \frac{c\tau}{2}\begin{bmatrix} 1 \\ e_1 \end{bmatrix}, \tag{25}$$

where we have made use of the one-way range vector

$$r_1 = \frac{c\tau}{2}e_1. \tag{26}$$

The second four-vector connects the events of laser pulse emission on the spacecraft and the position of the target body (with respect to the spacecraft) at laser pulse reflection at $t_1 + \tau/2$

$$\mathbf{r}_s(t^*) = \begin{bmatrix} c(t^* - t_1) \\ r_s(t^*) \end{bmatrix} = \begin{bmatrix} 0 \\ r_s(t_1) \end{bmatrix} + \begin{bmatrix} c\tau/2 \\ v_{12}\tau/2 \end{bmatrix}. \tag{27}$$

Note, as we have assumed that v_{12} is constant we can simply compute the position vector between spacecraft and target by $r_s(t^*) = r_s(t_1) + v_{12}\tau/2$.
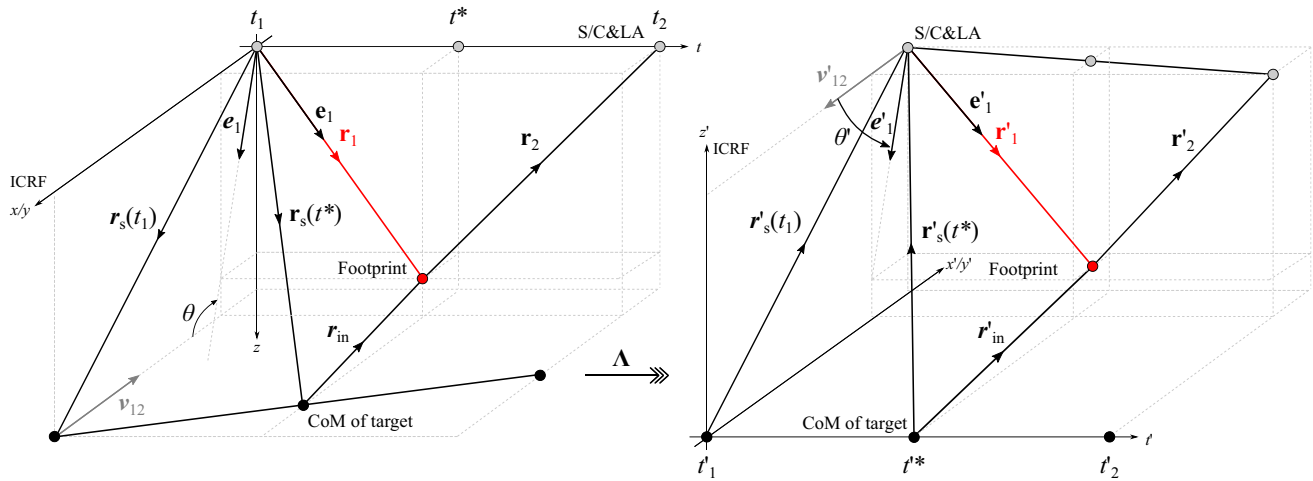
Fig. 4 Scheme of the special relativity model (SRM). The left and right panels denote the measurement process as observed from the spacecraft and the target body, respectively. Vectors printed in bold denote (space–time) four-vectors and those printed in bold and italic denote regular spatial vectors, i.e., with zero time component. $\boldsymbol{r}_{\text{in}}$ is the positional vector of the bounce point with respect to the target body. $\mathbf{r}_1$ is the one-way four-vectors of the transmission leg. $\mathbf{e}_1$ is the four-vector representation of the boresight direction $\boldsymbol{e}_1$. $\mathbf{r}_s(t^*)$ is the four-vector of the target body with respect to the spacecraft at the reflection time t^*. $\boldsymbol{v}_{12}$ is the relative velocity vector of the target body with respect to the spacecraft. t is the proper time of the spacecraft. The definitions are vice versa for the quantities with primes in the right panel

By computing the difference of these two four-vectors, we obtain the four-vector for the footprint

$$
\begin{aligned}
\mathbf{r}_{\text{in}} &= \mathbf{r}_1 - \mathbf{r}_s(t^*) \\
&= \begin{bmatrix} c\tau/2 \\ \boldsymbol{r}_1 \end{bmatrix} - \begin{bmatrix} c(t^* - t_1) \\ \boldsymbol{r}_s(t^*) \end{bmatrix} = \begin{bmatrix} c\tau/2 - c\tau/2 \\ \boldsymbol{r}_1 - \boldsymbol{r}_s(t^*) \end{bmatrix} \\
&= \begin{bmatrix} 0 \\ \boldsymbol{r}_1 - \boldsymbol{r}_s(t_1) - \boldsymbol{v}_{12}\tau/2 \end{bmatrix} = \begin{bmatrix} 0 \\ \boldsymbol{r}_{\text{in}} \end{bmatrix}.
\end{aligned} \tag{28}
$$

Thus, observed from the spacecraft the laser pulse is reflected at $t^* = t_1 + \tau/2$ and the footprint coordinates are $\boldsymbol{r}_{\text{in}} = \boldsymbol{r}_1 - \boldsymbol{r}_s(t^*)$. In order to obtain the corresponding counterparts of quantities as observed from the target body, we need to apply a Lorentz transformation.

The proper Lorentz transformation boost matrix $\boldsymbol{\Lambda}$ from the spacecraft quasi-inertial reference frame to the target body quasi-inertial reference frame can be written as (Nolting 2013)

$$
\begin{aligned}
\boldsymbol{\Lambda} &= \begin{bmatrix} \gamma & -\gamma\boldsymbol{\beta}^{\text{T}} \\ -\gamma\boldsymbol{\beta} & \mathbf{L} \end{bmatrix} \\
&= \begin{bmatrix}
\gamma & -\gamma\beta_x & -\gamma\beta_y & -\gamma\beta_z \\
-\gamma\beta_x & 1+(\gamma-1)\frac{\beta_x^2}{\beta^2} & (\gamma-1)\frac{\beta_x\beta_y}{\beta^2} & (\gamma-1)\frac{\beta_x\beta_z}{\beta^2} \\
-\gamma\beta_y & (\gamma-1)\frac{\beta_y\beta_x}{\beta^2} & 1+(\gamma-1)\frac{\beta_y^2}{\beta^2} & (\gamma-1)\frac{\beta_y\beta_z}{\beta^2} \\
-\gamma\beta_z & (\gamma-1)\frac{\beta_z\beta_x}{\beta^2} & (\gamma-1)\frac{\beta_z\beta_y}{\beta^2} & 1+(\gamma-1)\frac{\beta_z^2}{\beta^2}
\end{bmatrix},
\end{aligned} \tag{29}
$$

where β is the norm of $\boldsymbol{\beta} = -\boldsymbol{v}_{12}/c$ and the Lorentz factor γ is defined by

$$
\gamma = \frac{1}{\sqrt{1-\beta^2}}. \tag{30}
$$

Note that $\boldsymbol{v}_{12}$ denotes the relative velocity vector of the target body with respect to the spacecraft, which is constant given the assumptions made at the beginning. The matrix $\mathbf{L}$ is the sliced (spatial) part of $\boldsymbol{\Lambda}$ and can be expressed as

$$
\mathbf{L} = \mathbf{I} + \frac{\gamma-1}{\beta^2}\boldsymbol{\beta}\boldsymbol{\beta}^{\text{T}}, \tag{31}
$$

where $\mathbf{I}$ represents the 3×3 identity matrix.

Now the four-vector of the footprint as observed from the target body can be obtained by

$$
\begin{aligned}
\mathbf{r}'_{\text{in}} &= \boldsymbol{\Lambda} \cdot \mathbf{r}_{\text{in}} = \boldsymbol{\Lambda} \begin{bmatrix} 0 \\ \boldsymbol{r}_{\text{in}} \end{bmatrix} \\
&= \begin{bmatrix} -\gamma\boldsymbol{\beta} \cdot \boldsymbol{r}_{\text{in}} \\ \mathbf{L} \cdot \boldsymbol{r}_{\text{in}} \end{bmatrix} = \begin{bmatrix} -\gamma\boldsymbol{\beta} \cdot \boldsymbol{r}_{\text{in}} \\ \mathbf{L} \cdot (\boldsymbol{r}_1 - \boldsymbol{r}_s(t^*)) \end{bmatrix}.
\end{aligned} \tag{32}
$$

Finally the $\boldsymbol{r}'_{\text{in}}$ can be expressed as

$$
\begin{aligned}
\boldsymbol{r}'_{\text{in}} &= \mathbf{L} \cdot (\boldsymbol{r}_1 - \boldsymbol{r}_s(t^*)) = \boldsymbol{r}_1 - \boldsymbol{r}_s(t^*) \\
&\quad + \frac{\gamma-1}{\beta^2}\left(\boldsymbol{\beta}\boldsymbol{\beta}^{\text{T}}\right) \cdot (\boldsymbol{r}_1 - \boldsymbol{r}_s(t^*)),
\end{aligned} \tag{33}
$$

Note that the involved quantities $\boldsymbol{r}_s(t^*)$ and $\boldsymbol{r}_1$ are still those which were observed from the spacecraft. In particular, for

the time of reflection t^* in the proper timescale of the spacecraft it holds $t^* = t_1 + \tau/2$. However, to obtain the body-fixed position of the footprint on the surface of the target body with Eq. (1) we need to convert τ to TDB timescale. This aspect is discussed in more detail in Section A in Appendices.

2.5 Relation between PAM and SRM

Theoretically, the pointing aberration can be straightforwardly derived using the Lorentz velocity transformation, while the Lorentz velocity transformation can be inferred from the Lorentz transformation by calculation of the derivative with respect to time on both sides of the equation. Thus, the pointing aberration correction could also be deduced from the Lorentz transformation in its general form as represented by Eq. (29) and PAM with the targets as the observers should be nearly identical to SRM with difference on the order of $\mathcal{O}(\beta^2)$ in terms of the pointing correction. Here, we carry out a two-step analysis to tap into the relation between these two models: (1) Simplify and approximate the resultant formula Eq. (33) from SRM and (2) deduce the pointing correction angle $\Delta\theta'$ inferred from SRM to see whether it equals the pointing aberration correction $\Delta\theta$ as in PAM.

For (1), we first expand the expression for $\mathbf{L}$ in Eq. (31) as series of β

$$\mathbf{L} = \mathbf{I} + \frac{1}{2}\boldsymbol{\beta}\boldsymbol{\beta}^{\mathrm{T}} + \frac{3}{8}\beta^2 \boldsymbol{\beta}\boldsymbol{\beta}^{\mathrm{T}} + \mathcal{O}(\beta^6), \tag{34}$$

With that, Eq. (33) becomes

$$\mathbf{r}'_{\mathrm{in}} = \mathbf{r}_1 - \mathbf{r}_{\mathrm{s}}(t^*) + \frac{1}{2}\boldsymbol{\beta}\boldsymbol{\beta}^{\mathrm{T}}\mathbf{r}_1 - \frac{1}{2}\boldsymbol{\beta}\boldsymbol{\beta}^{\mathrm{T}}\mathbf{r}_{\mathrm{s}}(t^*) + \mathcal{O}(\beta^4). \tag{35}$$

Recalling that $\mathbf{r}_1 = r_1 \mathbf{e}_1$, we obtain

$$\frac{1}{2}\boldsymbol{\beta}\boldsymbol{\beta}^{\mathrm{T}}\mathbf{r}_1 = \frac{1}{2}r_1 \boldsymbol{\beta}\boldsymbol{\beta}^{\mathrm{T}}\mathbf{e}_1 = \frac{1}{2}\beta r_1 \cos\theta \boldsymbol{\beta}. \tag{36}$$

Rearranging terms in Eq. (35) and neglecting $\boldsymbol{\beta}\boldsymbol{\beta}^{\mathrm{T}}\mathbf{r}_{\mathrm{s}}(t^*)$ lead to

$$\mathbf{r}'_{\mathrm{in}} \approx r_1 \left(\mathbf{e}_1 + \frac{1}{2}\beta \cos\theta \boldsymbol{\beta} \right) - \mathbf{r}_{\mathrm{s}}(t^*). \tag{37}$$

Compared to the obtained result in PAM, we find that the boresight direction is now corrected by $\mathbf{e}_1 + \beta \cos\theta \boldsymbol{\beta}/2$. Note that the direction of $\mathbf{r}_{\mathrm{s}}(t^*)$ is opposite to the one used in SMM and PAM. The one-way range r'_1 can be approximated to

$$r'_1 = |\mathbf{L}\,\mathbf{r}_1| = r_1 \left(1 + \frac{1}{2}\beta^2 \cos^2\theta \right) + \mathcal{O}(\beta^4). \tag{38}$$

The maximum radius error associated with this approximation can be given by

$$\begin{aligned}
\Delta \|\mathbf{r}_{\mathrm{in}}\| &\leq (\gamma - 1) \left\| \boldsymbol{\beta}\boldsymbol{\beta}^{\mathrm{T}} \cdot (\mathbf{r}_1 - \mathbf{r}_{\mathrm{s}}(t^*)) \right\| \\
&\leq (\gamma - 1) \left\| \boldsymbol{\beta}\boldsymbol{\beta}^{\mathrm{T}} \right\| \|\mathbf{r}_1 - \mathbf{r}_{\mathrm{s}}(t^*)\| \\
&< \beta^2 \|\mathbf{r}_1 - \mathbf{r}_{\mathrm{s}}(t^*)\|.
\end{aligned} \tag{39}$$

Thus, this approximation error is solely related to the relative velocity of the spacecraft with respect to the target and to the radius of the target at the footprint.

For (2), we first apply the Lorentz transformation on the one-way range four-vector $\mathbf{r}_1$ from Eq. (25)

$$\mathbf{r}'_1 = \boldsymbol{\Lambda} \cdot \mathbf{r}_1 = \frac{c\tau}{2} \boldsymbol{\Lambda} \cdot \begin{bmatrix} 1 \\ \mathbf{e}_1 \end{bmatrix} = \frac{c\tau}{2} \begin{bmatrix} \gamma (1 - \boldsymbol{\beta} \cdot \mathbf{e}_1) \\ -\gamma\boldsymbol{\beta} + \mathbf{L} \cdot \mathbf{e}_1 \end{bmatrix}. \tag{40}$$

The time component of the four-vector denotes the ToF τ' as observed by the target body

$$\tau' = \tau\gamma (1 - \boldsymbol{\beta} \cdot \mathbf{e}_1) = \tau\gamma (1 - \beta \cos\theta), \tag{41}$$

which is the classical equation of time dilatation. The spatial component $\mathbf{e}'_1$ is the corrected boresight vector and can be expressed as

$$\mathbf{e}'_1 = \mathbf{L} \cdot \mathbf{e}_1 - \gamma\boldsymbol{\beta} = \mathbf{e}_1 + \left[(\gamma - 1) \cos\theta - \gamma\beta \right] \frac{\boldsymbol{\beta}}{\beta}. \tag{42}$$

The magnitude of $\mathbf{e}'_1$ is then constrained to be

$$e'_1 = \sqrt{\sin^2\theta + \gamma^2(\cos^2\theta - 2\beta \cos\theta + \beta^2)}, \tag{43}$$

which is always less than unity due to the length contraction effect induced by the special relativity. As in previous derivations, θ represents the angular separation between the relative velocity vector of the spacecraft with respect to the target body $\mathbf{v}_{12}$ and $\mathbf{e}_1$ (see also Fig. 3). Finally, the pointing correction by SRM $\Delta\theta'$ can be calculated as the angular separation between $\mathbf{e}'_1$ and $\mathbf{e}_1$ as

$$\begin{aligned}
\Delta\theta' &= \arccos\left(\frac{\mathbf{e}_1 \cdot \mathbf{e}'_1}{e'_1} \right) \\
&= \arccos\left(\frac{1 + \left[(\gamma - 1) \cos\theta - \gamma\beta \right] \cos\theta}{e'_1} \right) \\
&= \beta \sin\theta + \mathcal{O}(\beta^2) \approx \frac{v_{12}}{c} \sin\theta.
\end{aligned} \tag{44}$$

Thus, for $\beta_{12} \ll 0$ the derived expression for $\Delta\theta'$ coincides with $\Delta\theta$ from PAM (Eq. (19)), indicating that SRM can also be reduced to PAM if we assume that the relative velocity of the spacecraft with respect to the observer $\mathbf{v}_{12}$ is small.

2.6 Post-correction of the geolocation

As has already been stated, the performance of the geolocation models described above is often compromised by significant unmodeled orbit, attitude errors and less precise rotational parameters that are required to transform the footprint inertial coordinates to body-fixed ones, especially in the planetary case. Due to the lack of a ground truth for validation and calibration on planetary bodies, the most common approaches to post-correct the geolocation are the cross-over analysis (e.g., Neumann et al. 2001; Hu et al. 2013) and registration to optical stereoscopic Digital Terrain Models (DTMs) (e.g., Gläser et al. 2013; Barker et al. 2016). For MOLA, Neumann et al. (2001) has done a global cross-over analysis with corrections parameterized by slowly varying functions to adjust the tracks in 3D and to post-correct for residual spacecraft orbit, timing and pointing errors. The accuracy of individual footprints after the global cross-over analysis of MOLA is reported to be about 1 m radially and within 100 m laterally (Neumann et al. 2001).

3 Application to MOLA

3.1 Selected profiles and preprocessing

The MGS MOLA was inherited from the Mars Observer Laser Altimeter for which the requirements were a precision of 1.5 m and an accuracy of 30 m accuracy (Zuber et al. 1992). Enabled by improved electronics (Abshire et al. 2000) and precision gravity analysis and orbit determination (Lemoine et al. 2001), the performance of the MGS MOLA was substantially improved to be about 30 cm in precision over smooth terrain. The profile analysis of MOLA footprints after the cross-over analysis by Neumann et al. (2001) enabled the detection of the temporal variations in seasonal CO_2 ice/snow depth (Smith et al. 2001b). Up to the current day, MOLA data are still used extensively for geological and geophysical applications (Robbins and Hynek 2013; Heavens 2017; Parro et al. 2017). The MOLA Precision Experiment Data Records (PEDR) dataset Version L (Smith et al. 2003b, released on May 27, 2003) includes a total of more than 8600 valid profiles acquired in the mapping and extended phases from March 1999 to June 2001. It contains shot emission times, one-way ranges, laser altimeter pointing, as well as range corrections and other instrument and observation characteristics. For this study, five profiles in the mapping phase numbered orbit 1000, 3000, 5000, 7000 and 8000 have been selected for testing. The locations of the selected profiles are shown in Fig. 5. They cover latitudes of up to 86°S/N due to the inclination of the MGS frozen orbit and nadir-oriented configuration of MOLA. Some key measurement characteristics corresponding to these selected

profiles are visualized in Fig. 6. Due to the near-circular orbit during the mapping and extended phases, the relative velocity of MGS with respect to the CoM of Mars is around 3.4 km/s. The ranging distance slightly increases from about 370 km at the South Pole to 440 km at the North Pole. Given the aforementioned MOLA one-way ranging distance (thus ToF) and relative velocity of MGS, a motion of 8 to 10 m of the spacecraft with respect to Mars during ToF can be expected. In addition, MOLA remained nadir-pointed with off-nadir angle less than 1° during operation. In the PEDR processing, flagged noise returns and shots with missing attitude information have been excluded from the analysis. Further, corrections due to the detector response and range walk have been applied (Neumann et al. 2001). These range corrections are on the order of meters. Besides timing biases specific to MOLA, including the MOLA internal timing bias of 117.1875 ms, the CK time tag adjustment bias of -1.15 s has been accounted for (Neumann et al. 2001).

3.2 Comparison of SRM and PAM

We have theoretically proved that SRM can reduce to PAM given some assumptions in Sect. 2.5. Here, SRM and PAM are compared in the case of MOLA for verification. The differences of SRM with respect to PAM with Mars as observer (supplied with the attitude information and refined orbit model from NAIF (Konopliv et al. 2006)) are within 0.1 mm laterally and 3 mm radially (Fig. 7). Furthermore, the maximum approximation errors in radius as indicated in Eq. (39) are estimated to be ∼0.5 mm for MOLA profiles. These errors are relatively small compared to the differences between SRM and PAM as shown in Fig. 7. Thus, the effect of the special relativity could be well compensated by accounting for a simple pointing aberration correction. We then investigate the impact of this pointing aberration on the MOLA geolocation.

3.3 Impact of pointing aberration

The MOLA PEDR dataset has adopted SMM with Mars as the observer for the geolocation (Smith et al. 2003b). To investigate the improvement that can be achieved by solely incorporating the pointing aberration correction, the model outputs of PAM and SMM, with both using Mars as the observer, are compared in Fig. 8. The lateral differences do not show much variation and slowly increase from 4 m at south to a maximum of 5 m toward the north. The magnitudes of the radial differences peak at about 3 cm nearly midway between the equator and the poles (although with different signs for the ascending and descending tracks) and gradually decrease to 0.5 cm toward both the northern and southern ends of the track. The maximum height biases at the crossover points of the ascending and descending tracks caused by

Fig. 5 Location of the selected five profiles with the color scale indicating the height with respect to the IAU2015 Mars ellipsoid with an equatorial radius of 3396.19 km and mean polar radius of 3376.20 km (Archinal et al. 2018). The background is the 463 m per pixel resolution global greyscale hillshade of the MOLA Mission Experiment Gridded Data Record (MEGDR) (Smith et al. 2003a) in a van der Grinten projection with a central meridian of 90°E
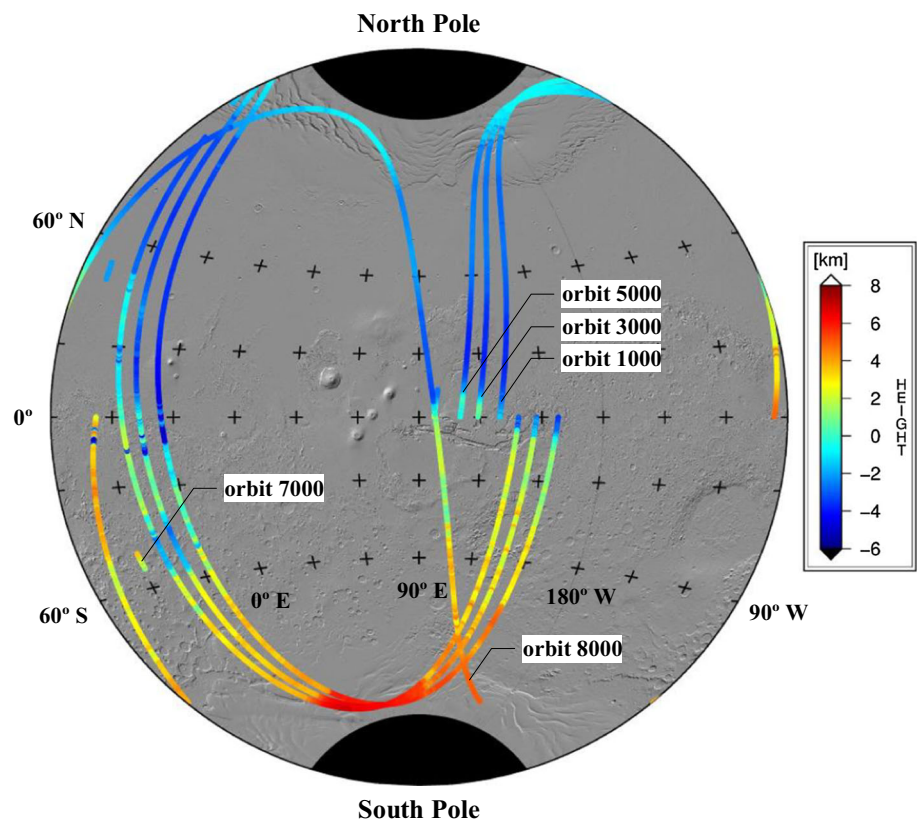

Fig. 6 MOLA measurement characteristics versus latitude for the selected profiles. Top: relative velocity with respect to the CoM of Mars. Center: one-way ranging distance. Bottom: off-nadir angle
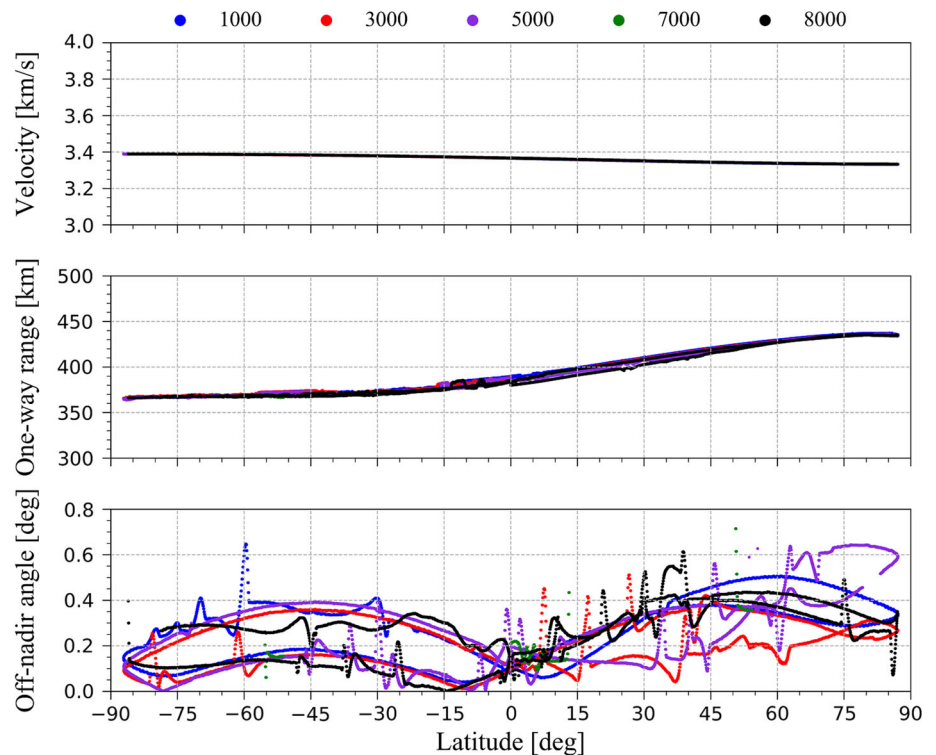
Fig. 7 Lateral (top) and radial (bottom) differences of SRM with respect to PAM with Mars as the observer for the selected MOLA profiles
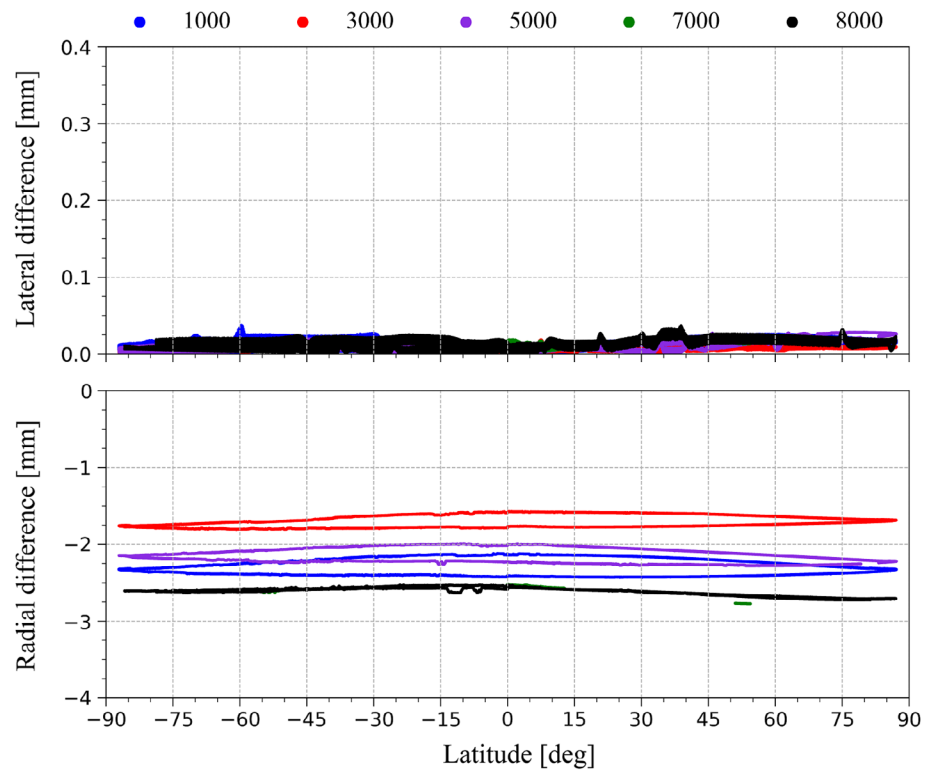

Fig. 8 Lateral (top) and radial (bottom) differences of PAM with Mars as observer with respect to SMM with Mars as observer for the selected profiles
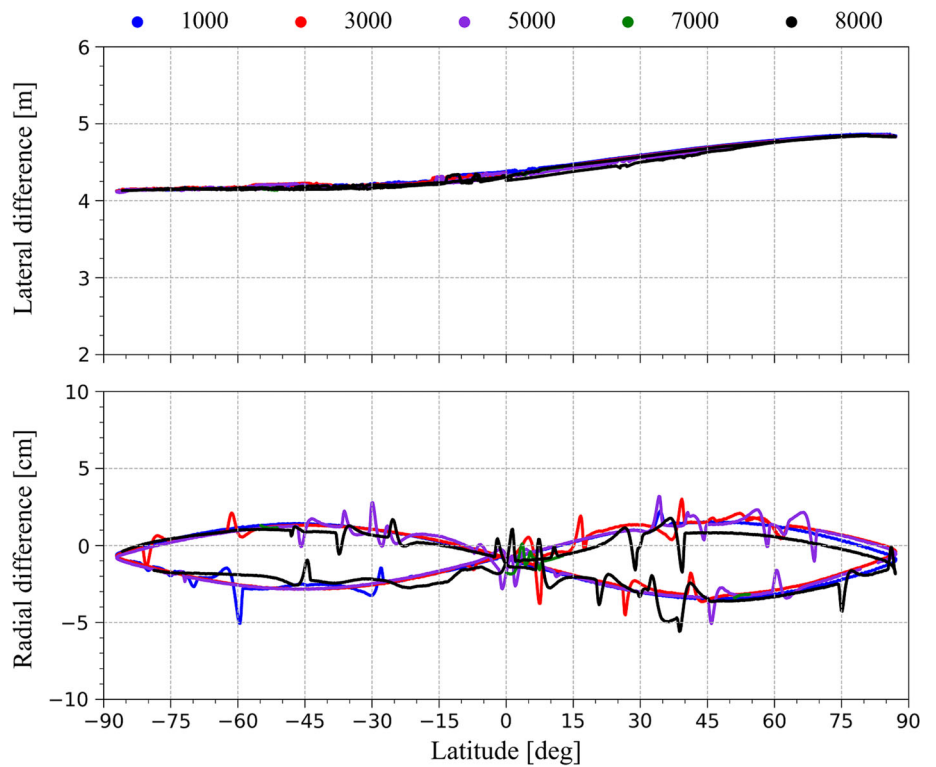
Table 1 Statistical summary of the comparison of different geolocation models applied to MOLA

Comparison pair	Lateral statistics			Radial statistics			
	Mean	RMS	Max	Mean	RMS	Max	Min
SRM versus PAM Mars as observer	0.0 mm	0.0 mm	0.0 mm	-2.2 mm	2.2 mm	-1.6 mm	-2.8 mm
PAM versus SMM Mars as observer	4.4 m	4.4 m	4.9 m	-0.8 cm	1.8 cm	3.2 cm	-5.6 cm

pointing aberration alone can thus only be 6 cm. Therefore, the effects of pointing aberration for circular orbits as the case of MOLA are relatively small. This has been expected, due to the nature of the circular orbit and the nadir pointing of the laser, especially when the relative velocity of the spacecraft and the observer (Mars) is small [compare Eq. (17) to Eq (24)].

3.4 Summary

The statistics for comparison of different geolocation models applied to MOLA dataset as shown in Figs. 7 and 8 is given in Table 1 for better interpretation. The relatively small numbers in the first row in the table indicates that the effect of the special relativity could be well compensated by accounting for a simple pointing aberration correction. The MOLA PEDR dataset has adopted SMM with Mars as the observer for the geolocation, neglecting the pointing aberration or special relativity effects. But the impact of this neglection is limited to 4 to 5 m laterally and up to ±3 cm (second row in Table 1). Compared to the accuracy of 100 laterally and approximately 1 m radially of the MOLA PEDR after the global cross-over analysis Neumann et al. (2001), the impact of the pointing aberration could thus be largely left unattended.

4 Application to MLA

4.1 Selected profiles and preprocessing

MLA had acquired one profile during each of the two Mercury flybys in 2008 and a total of 3270 profiles had been obtained in the 4 years from March 2011 to April 2015 in the orbital phase. Here, the MLA Reduced Data Record (RDR) MESSSMLA2001 dataset is utilized for the analysis (Neumann 2016). These records contain among others the shot ToF, firing time, instrument alignment, spacecraft orientation and quality flags. Here, apart from the two equatorial flyby profiles numbered 0801141902 and 0810060836, five other profiles numbered 1104010231, 1204011915, 1304010004, 1404011002 and 1504012318 have been selected out for tests. These 10-digit naming codes correspond to the Coordinated Universal Time (UTC) time when the first shot in the respective track was recorded. The distribution of the

selected seven profiles on the surface of Mercury is shown in Fig. 9. The two flyby profiles run approximately along the equator, while the other orbital profiles cluster in the northern hemisphere due to MESSENGER's eccentric, high inclination orbit and the limitation of the MLA ranging distance. The spacecraft speed, altitude and off-nadir pointing angle when these profiles were acquired are plotted versus the longitude (flyby profiles) and latitude (orbital profiles) in Fig. 10. Note that the flyby profile 0810060836 has been offset by -180° in longitude to fit in the depicted range; the same is done in Figs. 11, 12 and 13. The relative velocity of MESSENGER with respect to the CoM of Mercury of the two flyby profiles is located at relatively high values with 6 to 7 km/s compared to 3 to 4 km/s for the orbital profiles. The one-way ranging distance culminates at 1500 km for the flyby profiles, while for most of the orbital profiles it gradually increases toward the lower latitudes to a maximum of 1000 km. Constrained by the fact that MESSENGER should always have its sunshade faced to the Sun, off-nadir angles generally increase southward and can be as high as 60°, but can be almost zero for profiles acquired from a dawn–dusk orbit, as profile 1304010004 marked in blue–violet in our case (Fig. 10). The large variations of the measuring characteristics between different orbital profiles are a result of the orbit correction maneuvers (OCMs) and orbital evolution due to various perturbing forces (Mazarico et al. 2014b). For the preprocessing, erroneous returns and shots with missing laser start trigger time and pulse width have been filtered out. The range walk error of MLA (about 0.6 m under ideal conditions) is much smaller than that of MOLA (1 to 3 m) and is further mitigated by the usage of a variable-gain amplifier (VGA) gain control that allows MLA to accommodate the wide signal dynamic range resulting from the constantly changing spacecraft altitude during measurements. Therefore, the range walk error is neglected. Unlike MOLA, the corrections to the range offsets due to electronic delays have already been incorporated in the RDR ToF records, which vary with different channels and thresholds and can be up to tens of meters (Sun and Neumann 2015).

4.2 Recomputation of RDR MESSMLA2001

Based on SMM with the Solar System Barycenter (SSB) as the observer (supplied with the same attitude and orbit ker-

Fig. 9 Location of the seven selected profiles with the color scale indicating the height defined with respect to the IAU2015 Mercury sphere with a radius of 2439.4 km (Archinal et al. 2018). The background is the 250 m resolution Mercury Dual Imaging System (MDIS) global mosaic (Denevi et al. 2017) in a van der Grinten projection with a central meridian of 0°E
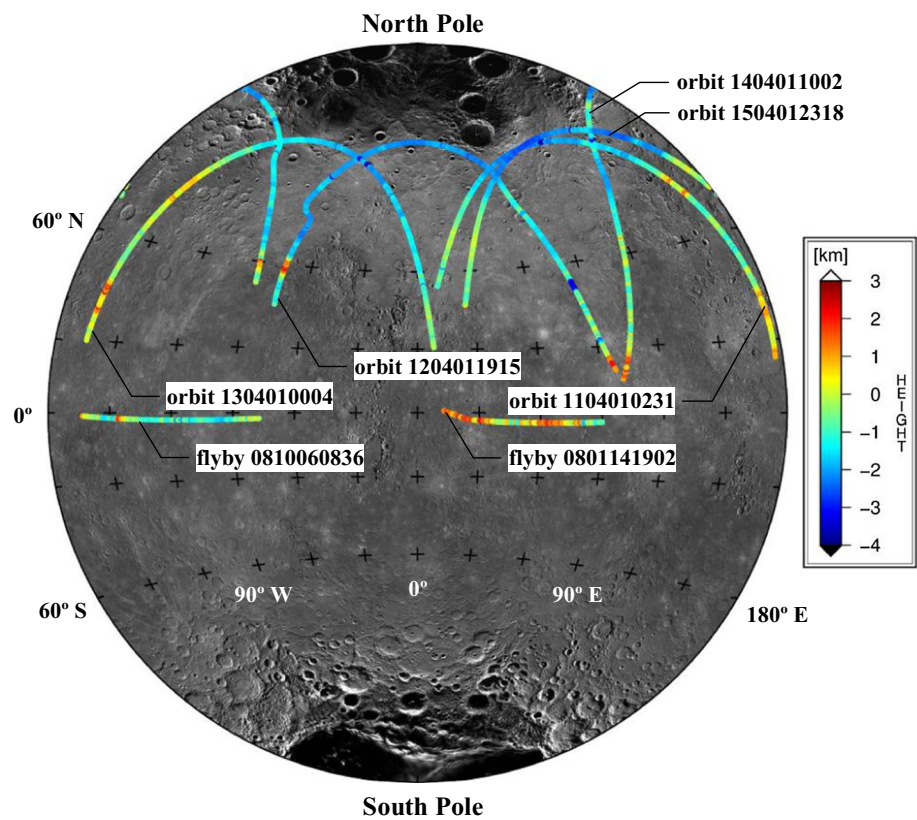
Fig. 10 MLA measuring characteristics with respect to longitude and latitude for the selected flyby and orbital profiles, respectively. Top: relative velocity with respect to the CoM of Mercury. Center: one-way ranging distance. Bottom: off-nadir angle
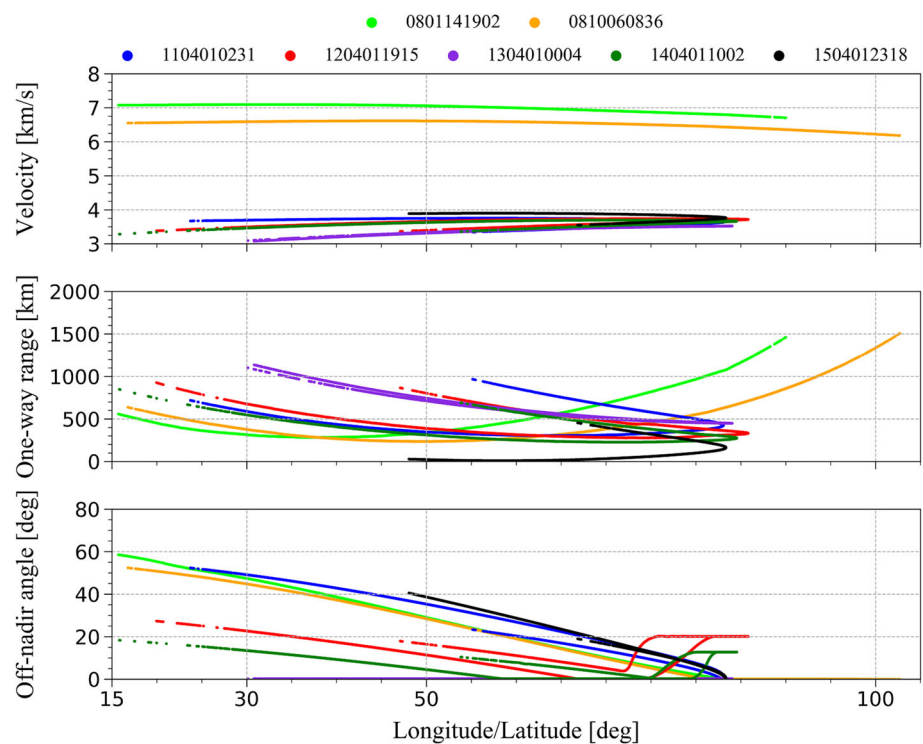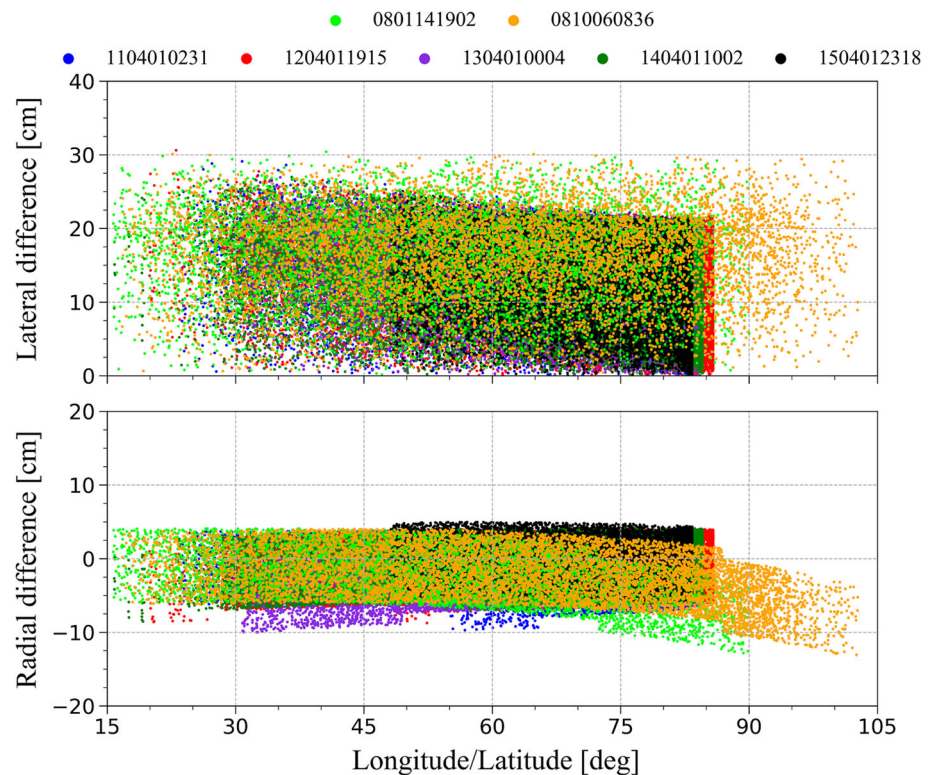
Fig. 11 Lateral (top) and radial (bottom) differences of SMM with the Solar System Barycenter (SSB) as observer with respect to RDR MESSMLA2001 for the selected profiles. The lateral difference is treated here and after as the geodetic distance along the IAU2015 Mercury sphere

nels that the RDR MESSMLA2001 has adopted and using the IAU2015 Mercury rotational model (Archinal et al. 2018)), we had managed to reproduce the RDR MESSMLA2001 locations. The recomputed footprint locations are then compared to the RDR MESSMLA2001 footprint positions as shown in Fig. 11. The residuals are below ∼30 cm laterally and range from ∼-15 cm to ∼5 cm radially. The residuals are fairly uniformly distributed within the band-like pattern for each profile, implying the cause to be the representation errors of relevant values by the RDR MESSMLA2001 files. Indeed, in these files the longitudes and latitudes in degree of the footprints are represented to five decimal places with radii in kilometers to four decimal places, and ToF measurements in nanoseconds are documented to first decimal place. Besides, the general trends of magnitudes on the order of several centimeters are due to the Shapiro delay that has been additionally taken care of in RDR MESSMLA 2001 by iteratively converging to the two-way light time solution (Neumann 2016) (see also Section C in Appendices). Thus, the RDR MESSMLA2001 is confirmed to have adopted SMM processing scheme in combination with the SSB being appointed as the observer with a small adjustment for Shapiro delay.

4.3 Comparison of SRM and PAM

As with MOLA in Sect. 3.2, SRM and PAM are compared in the case of MLA as well. The differences with Mercury as observer (supplied with the attitude and orbit kernels that adopted by the RDR MESSMLA2001) are within 2 cm laterally and 6 cm radially (Fig. 12). Mercury is chosen here as the observer for PAM in order to have a consistent comparison with SRM in which the target body is set as the observer for concise illustration. The maximum approximation errors as inferred by Eq. (39) are ∼0.5 mm for MLA orbital profiles, while this number increases to ∼1.3 mm for MLA flyby profiles. Like MOLA, these errors can be neglected compared to the differences between SRM and PAM as shown in Fig. 12. Thus, the effects of the special relativity could be aptly compensated by a pointing aberration correction. We then investigate the impact of this pointing aberration on the MLA geolocation.

4.4 Impact of pointing aberration

To investigate the improvement that can be achieved on the MLA RDR MESSMLA2001 by incorporating the pointing aberration correction, the model outputs of PAM and SMM both with the SSB as the observer (supplied with the attitude and orbit kernels that adopted by RDR MESSMLA2001) are compared in Fig. 13. The lateral differences vary from ∼0 m to up to more than 150 m for the orbital profiles and ∼20 m to ∼100 m for the flyby profiles. The maximum magnitude of the radial differences can be up to ∼25 m top for the orbital and ∼50 m for the flyby profiles. Note that the radial differences for ascending and descending tracks

Fig. 12 Lateral (top) and radial (bottom) differences of SRM with respect to PAM with Mercury as the observer for the selected MLA profiles
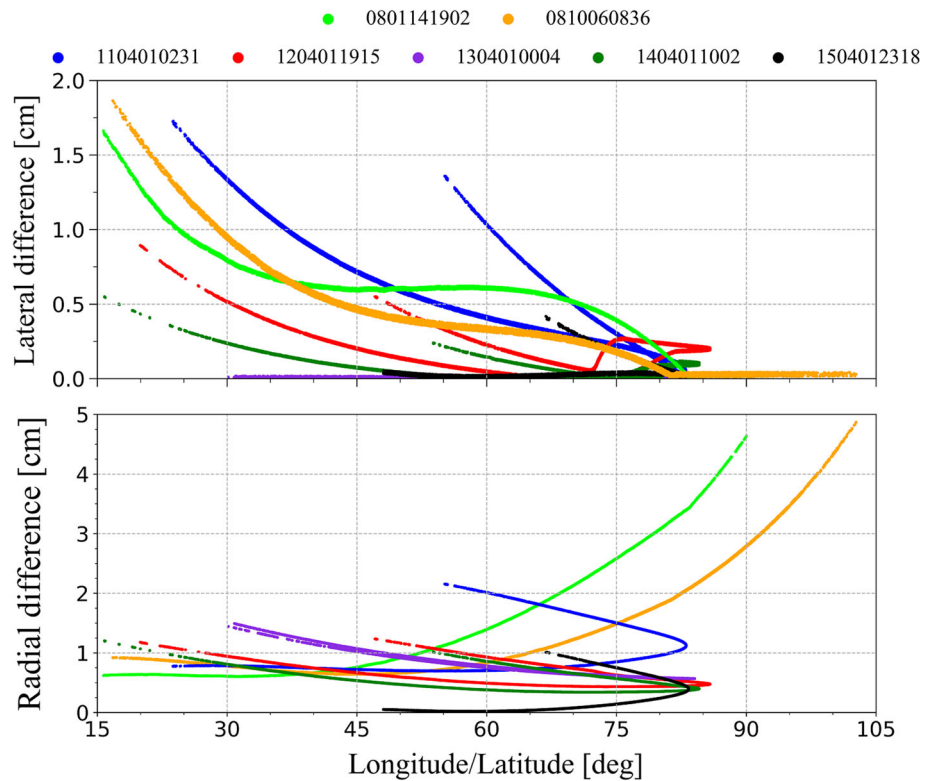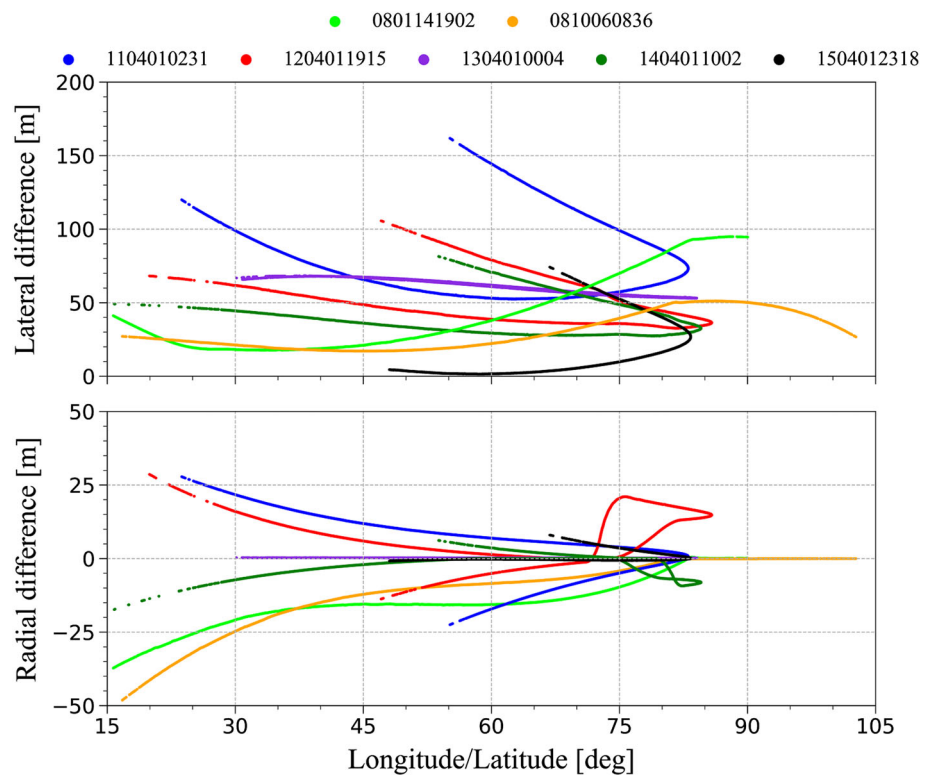

Fig. 13 Lateral (top) and radial (bottom) differences of PAM with the SSB as observer with respect to SMM with the SSB as observer for the selected profiles

of the orbital profiles are nearly symmetrically distributed around zero. The maximum height differences at the cross-over points of the ascending and descending tracks caused by pointing aberration can thus be ∼50 m in magnitude when approaching the equator. Owning to MESSENGER's highly eccentric orbit and significant MLA off-nadir pointing angle, these improvements by accounting for the relative velocity of MESSENGER with respect to SSB (∼47 km/s on average with maximum of ∼63 km/s) can be significantly larger than the ones of MOLA (Fig. 8). Thus, applying the correct model (PAM) can result in significant improvements of the MLA geolocation, especially for the flyby profiles [compare Eq. (17) to Eq. (24)].

To validate the improvements that could be brought by the pointing aberration correction in terms of RDR MESSMLA2001, we have compared the height misfits at cross-overs for RDR MESSMLA2001 and the reprocessed RDR MESSMLA2001 using PAM at the Shakespeare Quadrangle (H3) (22.5° to 65°N and 180° to 270°E). Before statistical analysis, these height discrepancies have been edited through a 3-sigma and 8-sigma iterative filtering process, respectively. As a result, 1.1% and 0.1% of these height misfits have been excluded from analysis for RDR MESSMLA2001 dataset (122206 left) and the reprocessed RDR MESSMLA2001 (95594 left), respectively. The histograms of these cross-over height misfits for RDR MESSMLA2001 and reprocessed RDR MESSMLA2001 are shown for comparison in Fig. 14. Note the long-tailing extreme large discrepancies for RDR MESSMLA2001 compared to the much more concentrated distribution for the reprocessed RDR MESSMLA2001. After accounting for the pointing aberration due to the relative velocity of MESSENGERER with respect to SSB, the mean and RMS of the height misfits at cross-overs have been improved from 11.8 m and 828.5 m to −2.8 m and 300.1 m, respectively, showcasing the significant improvements that could be brought to RDR MESSMLA2001 internal consistency after applying the pointing aberration correction. In addition, we have also compared the aforementioned results of RDR MESSMLA2001 to the new version of RDR MESSMLA2101 which has benefited from a refined MESSENGER orbit model derived from a simultaneously reprocessing of the radio tracking data with the MLA altimeter data (Neumann 2017). The histogram of RDR MESSMLA2101 is close to that of RDR MESSMLA2001 with mean of -13.4 m and RMS of 864.7 m from 117981 cross-overs, indicating that the errors induced by pointing aberration still remain in RDR MESSMLA2101.

4.5 Summary

The statistics for comparison of different geolocation models applied to MLA dataset as shown in Figs. 11, 12 and 13 are summarized in Table 2 for better interpretation. The centimeter-level numbers in the first row of the table indicate the MLA RDR MESSMLA2001 dataset has adopted SMM with SSB as the observer for the geolocation with a small adjustment for Shapiro delay, neglecting the pointing aberration correction to the boresight. In contrast to MOLA, the resultant geolocation errors can be up to ∼150 m laterally and ∼ ±25 m radially for the orbital profiles and up to ∼100 m laterally and ∼-50 m radially for the flyby profiles (third row of Table 2). Concerning cross-over height discrepancies at the Shakespeare Quadrangle (H3), the RMS could be reduced from 828.5 m for RDR MESSMLA2001 and 864.7 for RDR MESSMLA2101 to 300.1 m for the reprocessed RDR MESSMLA2001 incorporating the pointing aberration correction, nearly a threefold improvement in terms of self-consistency.

5 Discussion

The remarkable improvements in terms of self-consistency evaluated by the height misfits of cross-overs brought to RDR MESSMLA2001 by applying the pointing aberration correction as shown in Fig. 14 could be mainly attributed to the following factors: (1) along-track gaps up to 440 m between consecutive footprints means significant height interpolation distances to the cross-overs which would translate to large errors when the underlying terrain features rough crater rims and central peaks. (2) Large relative velocity of MESSENGER and SSB of magnitude ∼47 km/s on average could lead to significant pointing aberration correction and hence non-negligible lateral and radial shifts, especially toward the equator where one-way range and off-nadir angle generally increase (Figs. 10, 13). (3) Owing to the relative velocity vector of MESSENGER with respect to SSB being nearly perpendicular to the approximately meridian-parallel profiles at the Shakespeare Quadrangle (H3), the lateral shifts could have cross-track components, especially for profiles collected when MESSENGER was at noon–midnight orbit. These cross-track displacements are capable of shifting the intersection points dramatically upwards or downwards along the near-parallel profiles in question. (4) The radial shifts for ascending and descending profiles are nearly symmetrically distributed around zero; thus, the height misfits could be doubled at cross-overs (Fig. 13). As for RDR MESSMLA2101, although each MLA profile has been adjusted to an existing MLA DTM for refined MESSENGER orbit and MLA pointing, this postprocessing has not even slightly absorbed the pointing aberration errors. This could be due to the fact that a constant correction is applied to each MLA profile, while the pointing aberration errors as shown in Fig. 13 are largely nonlinear.

Three different kinds of general relativity effects on the geolocation, i.e., converting the ToF measurement in TDB
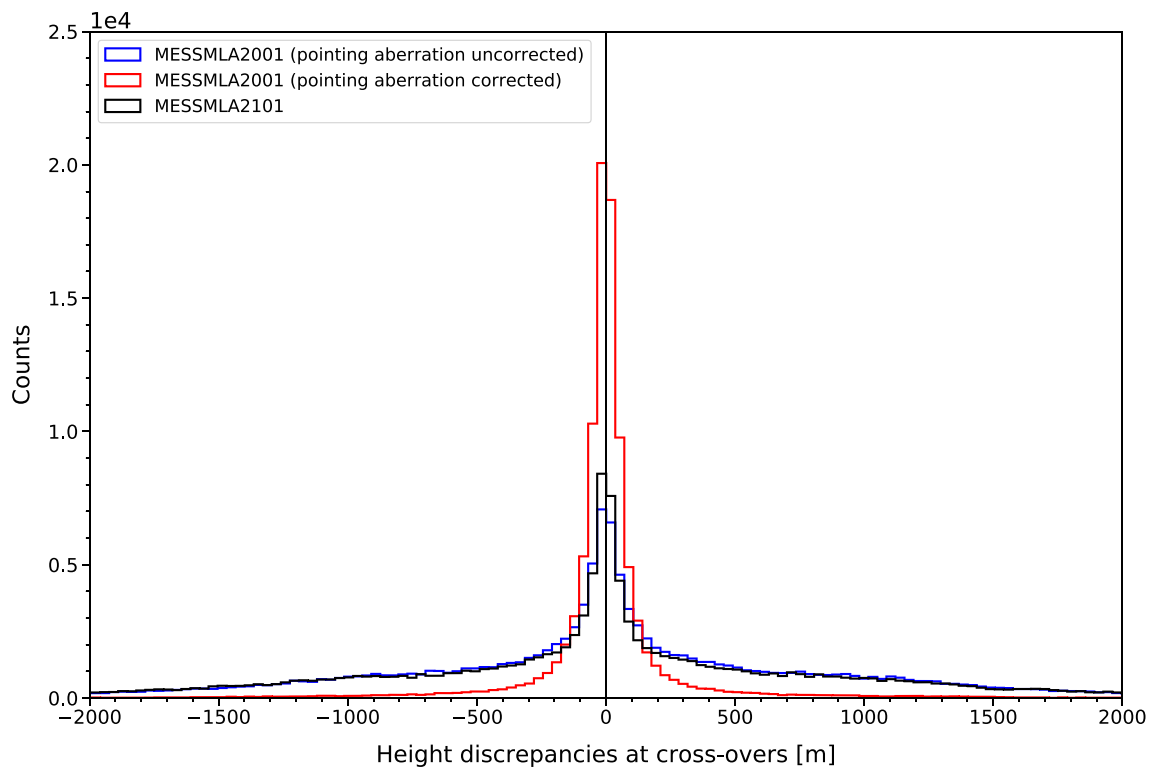
Fig. 14 Histogram of the height discrepancies at cross-overs for RDR MESSMLA2001 (blue), the reprocessed RDR MESSMLA2001 accounting for the pointing aberration (red) and RDR MESSMLA2101 (black) at the Shakespeare Quadrangle (H3)

Table 2 Statistical summary of the comparison of different geolocation models applied to MLA

Comparison pair	Lateral statistics			Radial statistics			
	Mean	RMS	Max	Mean	RMS	Max	Min
SMM SSB as observer versus MESSMLA2001	12.9 cm	14.2 cm	30.6 cm	− 1.6 cm	3.4 cm	5.0 cm	− 13.1 cm
SRM versus PAM Mercury as observer	0.2 cm	0.3 cm	1.9 cm	0.8 cm	0.9 cm	4.9 cm	0.0 cm
PAM versus SMM SSB as observer	46.9 m	52.1 m	161.8 m	− 0.4 m	8.2 m	28.6 m	− 48.1 m

scale to proper time of the spacecraft, errors of the laser pulse emission time stamps and the Shapiro delay, have also been examined and are detailed in Appendices. The maximum Shapiro delay of the transmit one-way leg has been estimated to be ∼6 mm and ∼9 cm for MOLA and MLA, respectively (Section C). Thus, for future laser altimeters to Mercury with long-ranging distance, e.g., BELA, the Shapiro delay has also to be compensated in the geolocation process.

6 Conclusion

We have presented a consistent and systematic formulation of three commonly used geolocation models which could account for the spacecraft's motion during the ToF of the laser pulse and pointing aberration. Then, the special relativity model is proposed to compensate for the special relativity effects. Furthermore, other conceivable effects (e.g., Shapiro delay) induced by general relativity have been discussed. These models have been applied to MOLA and MLA profiles as case examples. We have analytically demonstrated that the special relativity effects can be reduced to a simple pointing aberration correction given some assumptions. More importantly, ignoring the pointing aberration correction can lead to significant geolocation errors, especially when the laser altimeter is operating in an off-nadir configuration and the spacecraft is moving fast with respect to the observer body. This geolocation errors can be up to ∼150 m laterally and ∼ ±25 m radially when applied to the MLA orbital profiles. Concerning cross-over height discrepancies at the Shakespeare Quadrangle (H3), the RMS could be improved by a factor of 3 from 828.5 m for RDR MESSMLA2001 and 864.7 for RDR MESSMLA2101 to 300.1 m for RDR MESSMLA2001 corrected for the pointing aberration. This

paper can serve as a processing guide for future laser altimetry geolocation applications.

Compliance with ethical standards

Appendices

Here, we further discuss three other relativistic effects that have not been considered within SRM model which are generally small, but could be important to consider for future precise laser altimetry missions.

Appendix A: ToF measurement in TDB scale

In Sect. 2.4, τ denotes the proper ToF as measured in the spacecraft reference frame. But as mentioned before, due to the calibration of the spacecraft clock and laser altimeter USO by radio links to Earth, the documented ToF measurements are actually expressed in TDB scale τ_{TDB}, not as the proper time of the spacecraft. The conversion of τ_{TDB} to τ can be done via the time-dependent multiplicative scaling factor $\Omega_{\text{TDB}\rightarrow\text{proper}}$

$$\tau = \tau_{\text{TDB}}\Omega_{\text{TDB}\rightarrow\text{proper}}. \qquad (A.1)$$

$\Omega_{\text{TDB}\rightarrow\text{proper}}$ can be deduced by examining the rate deviation of spacecraft proper time and TDB with respect to Barycentric Coordinate Time (TCB) (Bauer et al. 2017)

$$\Omega_{\text{TDB}\rightarrow\text{proper}} = \frac{d_{\text{clock}}}{d_{\text{TCB}}}\bigg/\frac{d_{\text{TDB}}}{d_{\text{TCB}}}$$

$$= \frac{\sqrt{1 - 2\varphi_{\text{s/c}}/c^2 - |\boldsymbol{v}_{\text{s/c SSB}}|^2/c^2}}{1 - L_{\text{b}}}, \qquad (A.2)$$

with $\varphi_{\text{s/c}}$ being the total gravitational potential at the spacecraft's location, summed up over all bodies that cannot be neglected. $\boldsymbol{v}_{\text{s/c SSB}}$ represents the relative velocity vector of the spacecraft with respect to the SSB, while

$$1 - L_{\text{b}} = 1 - 1.50519768 \times 10^{-8} \qquad (A.3)$$

is the constant scaling of TDB with respect to the TCB $\frac{d_{\text{TDB}}}{d_{\text{TCB}}}$ (see Bauer et al. 2017, for details). If we assume that the magnitude of the relative velocity of the spacecraft with respect to SSB remains constant for the each measurement process, then the rate difference between the laser altimeter internal clock and TDB $\Omega_{\text{TDB}\rightarrow\text{proper}}$ is a constant. Since ToF measurements are typically expressed in TDB scale, Eq. (A.1) can be used to obtain the proper ToF τ as measured by the spacecraft and then further used in the calculations in Sect. 2.4.

Appendix B: Errors in the emission time

While the uncertainty of the time stamps in the MLA RDR dataset is well below 150μs which is mainly due to the Shapiro delay unmodeled in the MESSENGER timekeeping system (Cooper et al. 2012), the accuracy of the MGS Spacecraft Clock Coefficients Kernels (SCLKs), which convert the spacecraft clock ticks to Terrestrial Dynamical Time (TDT) time, is only 10 ms (corresponding to almost 30 m on the Martian surface) in the orbital phase (Neumann et al. 2006). This constitutes a significant source of geolocation error when considering that the mean errors of the refined MGS orbit have been reduced to less than 2 m (Konopliv et al. 2006). The laser timing is affected by the clock's drift and aging and also the relativity effects. If each of these factors could be accurately modeled, then the errors of the footprint emission time stamps could be significantly lowered, contributing to more rigorous and precise geolocation. Here, we have investigated the effects of gravitational potential at the spacecraft's location and its relative velocity with respect to the SSB on the MGS onboard clock rate as in Bauer et al. (2017). The result for the MGS mapping phase is plotted in the top panel of Fig. 15. Variations due to MGS's orbit around the Sun and Mars (see the inset) are visible with an average difference of $\sim 5.5 \times 10^{-9}$ s/s. Meanwhile, we have converted the TDT time tags documented in the MGS SCLKs to TDB timestamps and calculated the normalized deviation of the MGS onboard clock rate with respect to TDB (Fig. 15, bottom). Apparently, relativistic effects only account for a small fraction (a maximum of $\sim$0.06) of the total deviations (more than 110×10^{-9} s/s at the beginning of the map-

Fig. 15 MGS onboard clock rate deviation with respect to TDB during the MGS mapping phase. Top: rate deviation induced by the effects of relativity, the inset shows a zoomed view of the periodic variations inflicted by the gravity of Mars over one Earth day; Bottom: total rate deviation indicated by the MGS SCLK piecewise linear fitting. Grey shade denotes the period of the solar conjunction
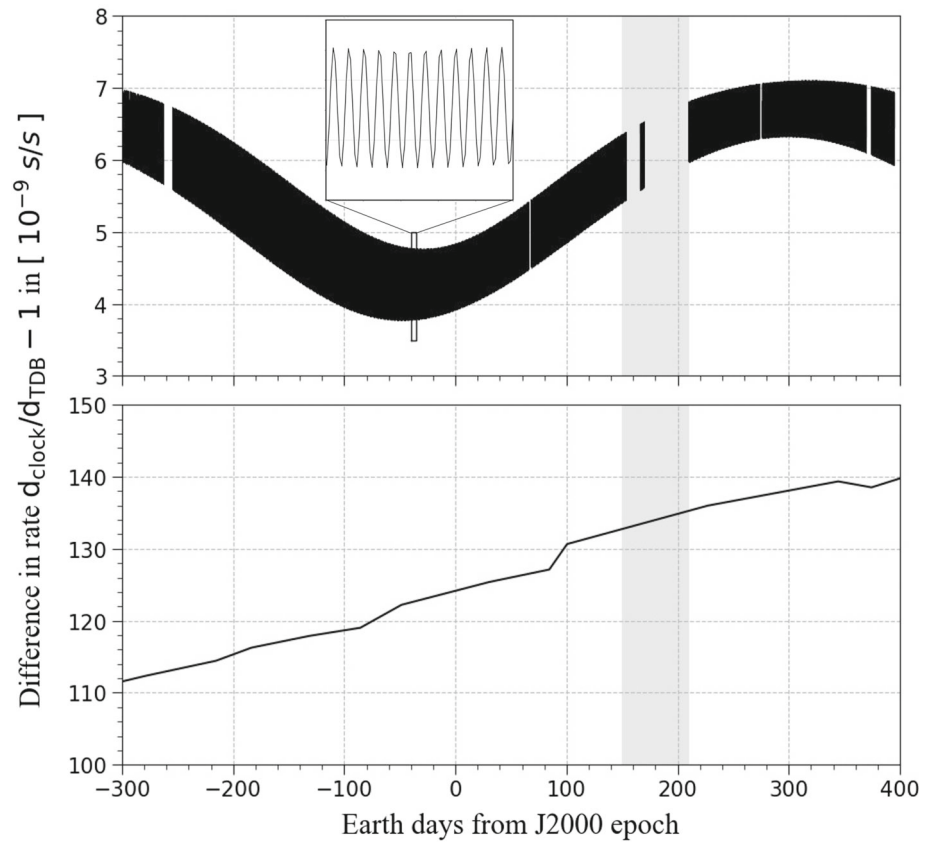
ping phase and increasing with mission elapsed time); the most influential factors are still the drift of the MGS clock itself. Unfortunately, the deterministic clock model was not revealed to the public, also gaps from solar conjunction and other causes exist; therefore, we did not attempt to further refine the MOLA emission time.

Appendix C: Shapiro delay

When the light propagates in a gravitational well, the coordinate velocity of light will be reduced to below c and a bending of the light path will occur. Thus, the light will travel an extra distance. These two effects will add up to the Shapiro delay (Shapiro 1964). We adopt the one-way light-time solution between any two points in the Solar System barycentric space–time frame to estimate the prolongation of the MLA one-way down-leg light path inflicted by Shapiro delay (Moyer 2005; Turyshev et al. 2010):

$$c(t_2 - t_1) = r_{12} + \sum_{B=1}^{n} \frac{(1+\gamma)\mu_B}{c^2}$$
$$\ln\left[\frac{r_1^B + r_2^B + r_{12}^B}{r_1^B + r_2^B - r_{12}^B}\right] + \mathcal{O}(c^{-4}). \qquad (A.4)$$

B denotes a celestial body in the Solar System. The μ_B term denotes the accumulating retardation effect of the celestial bodies. t_1 refers to the emission time of the laser pulse and t_2 is the reflection time on the surface of the target body. r_1 is the linear distance of the spacecraft with respect to the gravitational body at emission time, r_2 is the distance from the bounce point to the gravitational body at the reflection time. r_{12} is the relativistically uncorrected linear range of the transmit one-way leg. γ is one of the ten parameters in the parameterized post-Newtonian (PPN) formalism. μ_B is the standard gravitational parameter of a celestial body.

The potential upper limit of the impact of each gravitational body in the Solar System is estimated separately to infer the maximum delay MOLA and MLA might have experienced. For MOLA, mostly nadir-pointed in the mapping phase, the one-way distance r_{12} ranges from 368 to 438 km. We use the maximum distance for the error estimation. The Shapiro delay inflicted on the MOLA transmit one-way leg by the Sun is at its maximum when Mars is at its perihelion (25 November 1999). For simplicity, we focus on the two extreme cases, which are (1) Mars being in opposition to the MGS spacecraft and (2) the MGS spacecraft being in opposition to Mars (top left and top right in Fig. 16, respectively). In these two cases, r_1 and r_2 can be easily related to $\overline{R}$, d and r_{12} as embedded in the geometry. Here, $\overline{R}$ is the mean radius of Mars and d is the Mars–Sun distance at perihelion

Fig. 16 Top: two extreme cases used to constrain the maximum prolongation on the MOLA transmit leg by the Sun. Bottom: configuration where the MGS altitude and the gravitational delay impact of Mars maximize
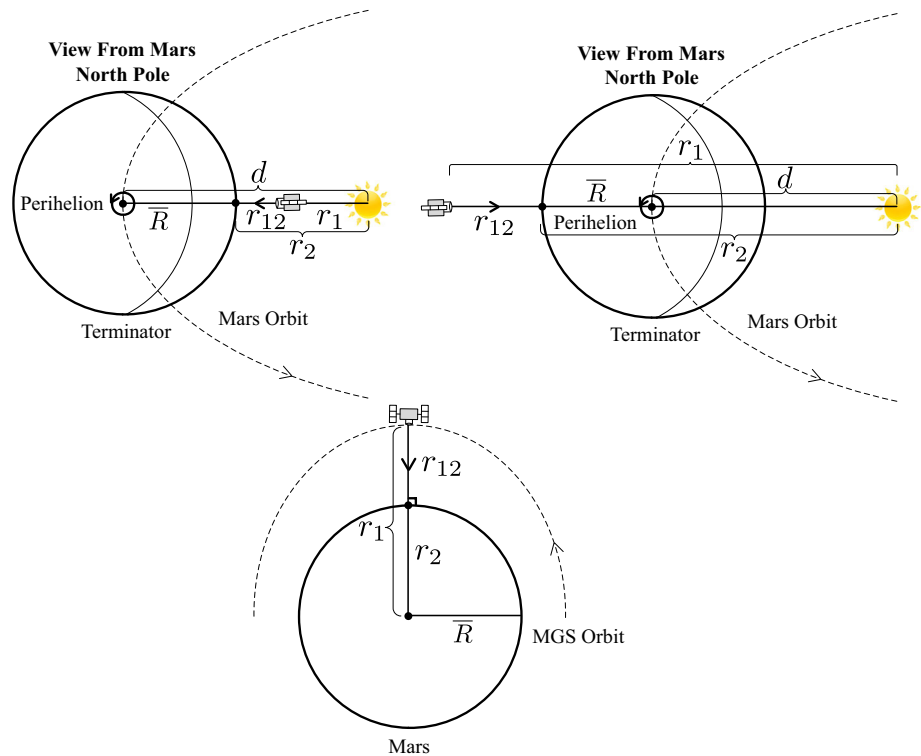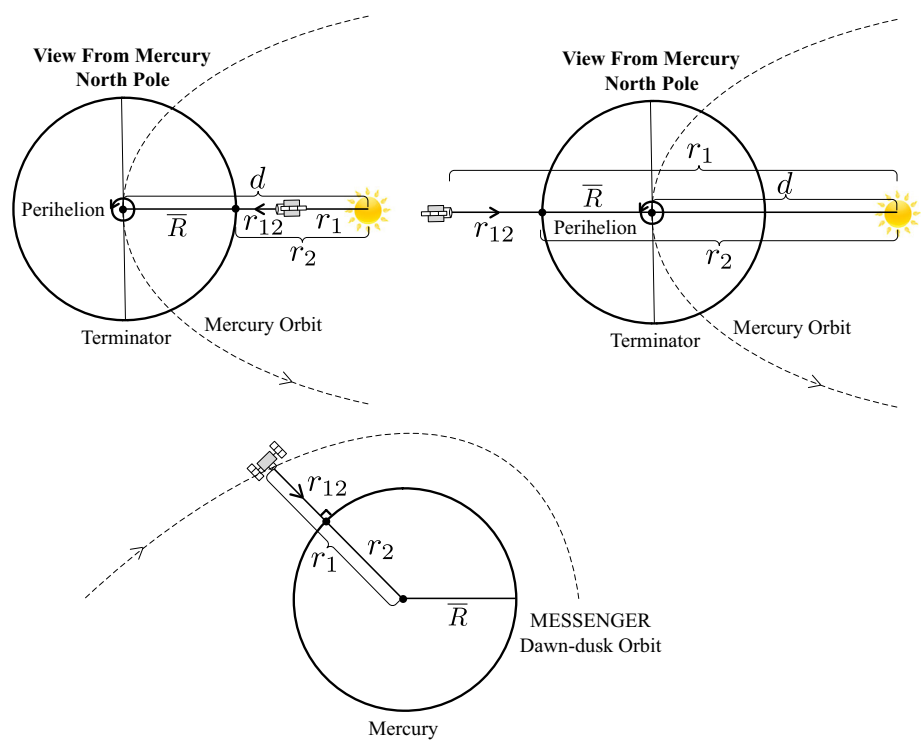

Fig. 17 Top: two extreme cases used to constrain the maximum prolongation on the MLA transmit leg induced by the gravitational field of the Sun. Bottom: configuration when the MLA ranging distance is the longest and the gravitational delay impact of Mercury peaks. Here, $\overline{R}$ is the mean radius of Mercury and d is the distance between Mercury's perihelion and the Sun

(see Fig. 16). Inserting these parameters into the second term of Eq. (A.4), both scenarios yield nearly identical maximum range prolongation of 6.3 mm as for the impact of the Sun. When it comes to Mars, assuming it to be a point source of gravity, then the impact peaks at 0.12 mm when MGS is at apoapsis where the maximum ranging distance is reached (over the North Pole, see bottom panel in Fig. 16). For other planets, the impacts are all at least two order of magnitudes smaller than the impact of Mars itself and can be neglected. Thus, the maximum prolongation exerted on MOLA's one-way range by all the gravitational bodies in the Solar System is less than 1 cm. Among MGS orbit and attitude errors and MOLA timing errors, the Shapiro delay for MOLA could thus be largely neglected during geolocation.

MLA can successfully perform range measurements up to 1500 km altitude, assuming nadir operation in an eccentric dawn–dusk orbit (Zuber et al. 2012). Thus, the MLA one-way distance of r_{12} is set to 1500 km to estimate the maximum gravitational delay MLA might experience. The maximum impact exerted by Sun occurs when Mercury is at perihelion. As with MOLA, we consider two extreme scenarios to constrain the magnitude (see Fig. 17). r_1 denotes the distance of the Sun to MESSENGER and r_2 denotes the distance of the Sun to the bounce point, which can be readily known given their simple geometric relations with respect to $\overline{R}$, d and r_{12}. Using the formalism discussed before, the two extreme cases yield similar range prolongation of 9.4 cm with a difference on the order of 0.01 mm; thus, the maximum gravitational delay of Sun on MLA one-way leg is ~ 9.4 cm. Similarly, for the impact of Mercury itself, the maximum is when MESSENGER is in a dawn–dusk orbit and the ranging distance reaches the maximum of 1500 km in a nadir pointing configuration (bottom plot in Fig. 17). The corresponding range prolongation for the transmit leg is then calculated to be 0.46 mm. For all other bodies, the impacts are all at least two order of magnitudes smaller than that of Mercury and can be neglected. Thus, the maximum prolongation exerted on MLA one-way range due to Shapiro delay is $\sim$9 cm. Future laser altimeter missions to Mercury with the aim of achieving centimeter-level ranging accuracy should take the Shapiro delay into careful consideration.

References

Abshire JB, Sun X, Afzal RS (2000) Mars Orbiter Laser Altimeter: receiver model and performance analysis. Appl Opt 39(15):2449–2460. https://doi.org/10.1364/AO.39.002449

Archinal BA, Acton CH, A'Hearn MF, Conrad A, Consolmagno GJ, Duxbury T, Hestroffer D, Hilton JL, Kirk RL, Klioner SA, McCarthy D, Meech K, Oberst J, Ping J, Seidelmann PK, Tholen DJ, Thomas PC, Williams IP (2018) Report of the IAU working group on cartographic coordinates and rotational elements: 2015. Celest Mech Dyn Astron 130(3):22. https://doi.org/10.1007/s10569-017-9805-5

Bae S, Schutz BE (2002) Geoscience Laser Altimeter System (GLAS) Precision Attitude Determination (PAD). Algorithm Theoretical Basis Documents (ATBD), pp 1–106

Barker MK, Mazarico E, Neumann GA, Zuber MT, Haruyama J, Smith DE (2016) A new lunar digital elevation model from the Lunar Orbiter Laser Altimeter and SELENE Terrain Camera. Icarus 273:346–355. https://doi.org/10.1016/j.icarus.2015.07.039

Bauer S, Hussmann H, Oberst J, Dirkx D, Mao D, Neumann GA, Mazarico E, Torrence MH, McGarry JF, Smith DE, Zuber MT (2017) Analysis of one-way laser ranging data to LRO, time transfer and clock characterization. Icarus 283:38–54. https://doi.org/10.1016/j.icarus.2016.09.026

Cooper SB, Jensen JR, Weaver GL (2012) MESSENGER onboard timekeeping accuracy during the first year in orbit at Mercury. In: 44th Annual precise time and time interval (PTTI) systems and applications meeting, pp 361–370

Daly MG, Barnouin OS, Dickinson C, Seabrook J, Johnson CL, Cunningham G, Haltigin T, Gaudreau D, Brunet C, Aslam I, Taylor A, Bierhaus EB, Boynton W, Nolan M, Lauretta DS (2017) The OSIRIS-REx Laser Altimeter (OLA) investigation and instrument. Space Sci Rev 212(1–2):899–924. https://doi.org/10.1007/s11214-017-0375-3

Denevi BW, Chabot NL, Murchie SL, Becker KJ, Blewett DT, Domingue DL, Ernst CM, Hash CD, Hawkins SE, Keller MR, Laslo NR, Nair H, Robinson MS, Seelos FP, Stephens GK, Turner FS, Solomon SC (2017) Calibration, projection, and final image products of MESSENGER's Mercury Dual Imaging System. Space Sci Rev 214(1):52. https://doi.org/10.1007/s11214-017-0440-y

Gläser P, Haase I, Oberst J, Neumann GA (2013) Co-registration of laser altimeter tracks with digital terrain models and applications in planetary science. Planet Space Sci 89:111–117. https://doi.org/10.1016/j.pss.2013.09.012

Heavens NG (2017) The reflectivity of Mars at 1064 nm: derivation from Mars Orbiter Laser Altimeter data and application to climatology and meteorology. Icarus 289:1–21. https://doi.org/10.1016/j.icarus.2017.01.032

Hu W, Di K, Liu Z, Ping J (2013) A new lunar global DEM derived from Chang'E-1 Laser Altimeter data based on crossover adjustment with local topographic constraint. Planet Space Sci 87:173–182. https://doi.org/10.1016/j.pss.2013.08.004

Hussmann H (2014) Laser altimetry and its applications in planetary science. In: Planetary geodesy and remote sensing, pp 51–75

Hussmann H, Lingenauber K, Kallenbach R, Enya K, Thomas N, Lara LM, Althaus C, Araki H, Behnke T, Castro JM, Henri M, Gerber T, Herranz M, Revilla D, Hüttig C, Ishibashi K, Jiménez J, Martínez I, Harald N, Noriyuki M, Hirotomo N, Jürgen N, Oshigami S, Pablo J, García R, Rodrigo J, Rösner K, Stark A, Steinbrügge G, Thabaut P, Kazuyuki T, Sebastian T, Wendler B, Wickhusen K, Willner K (2019) The Ganymede laser altimeter (GALA): key objectives, instrument design, and performance. CEAS Space J 11(4):381–390. https://doi.org/10.1007/s12567-019-00282-8

Konopliv AS, Yoder CF, Standish EM, Yuan DN, Sjogren WL (2006) A global solution for the Mars static and seasonal gravity, Mars orientation, Phobos and Deimos masses, and Mars ephemeris. Icarus 182(1):23–50. https://doi.org/10.1016/j.icarus.2005.12.025

Lemoine FG, Smith DE, Rowlands DD, Zuber MT, Neumann GA, Chinn DS, Pavlis DE (2001) An improved solution of the gravity field of Mars (GMM-2B) from Mars Global Surveyor. J Geophys Res Planets 106(E10):23359–23376. https://doi.org/10.1029/2000JE001426

Luthcke SB, Rowlands DD, Williams TA, Sirota M (2005) Reduction of ICESat systematic geolocation errors and the impact on ice sheet elevation change detection. Geophys Res Lett 32:3–6. https://doi.org/10.1029/2005GL023689

Luthcke SB, Pennington T, Rebold T, Thomas T (2019a) ATL03g ICESat-2 Receive Photon Geolocation (version 6). Algorithm Theoretical Basis Documents (ATBD), pp 1–53

Luthcke SB, Rebold T, Thomas T, Pennington T (2019b) GEDI Waveform Geolocation for L1 and L2 Products (version 1.0). Algorithm Theoretical Basis Documents (ATBD), pp 1–62

Magruder L, Silverberg E, Webb C, Schutz B (2005) In situ timing and pointing verification of the ICESat altimeter using a ground-based system. Geophys Res Lett. https://doi.org/10.1029/2005GL023504

Mazarico E, Neumann GA, Rowlands DD, Smith DE (2010) Geodetic constraints from multi-beam laser altimeter crossovers. J Geodesy 84(6):343–354. https://doi.org/10.1007/s00190-010-0379-1

Mazarico E, Barker MK, Neumann GA, Zuber MT, Smith DE (2014a) Detection of the lunar body tide by the Lunar Orbiter Laser Altimeter. Geophys Res Lett 41:2282–2288. https://doi.org/10.1002/2013GL059085

Mazarico E, Genova A, Goossens S, Lemoine FG, Neumann GA, Zuber MT, Smith DE, Solomon SC (2014b) The gravity field, orientation, and ephemeris of Mercury from MESSENGER observations after three years in orbit. J Geophys Res Planets 119(12):2417–2436. https://doi.org/10.1002/2014JE004675

Mizuno T, Kase T, Shiina T, Mita M, Namiki N, Senshu H, Yamada R, Noda H, Kunimori H, Hirata N, Terui F, Mimasu Y (2017) Development of the Laser Altimeter (LIDAR) for Hayabusa2. Space Sci Rev 208(1):33–47. https://doi.org/10.1007/s11214-015-0231-2

Moyer TD (2005) Formulation for observed and computed values of Deep Space Network data types for navigation, vol 3. Wiley, New York

Neumann GA (2016) Mercury Laser Altimeter (MLA) Planetary Data System (PDS) document. https://pds-geosciences.wustl.edu/messenger/mess-e_v_h-mla-3_4-cdr_rdr-data-v1/messmla_2001/document/mla_edr_to_cdr_to_rdr-gdr.pdf. Accessed 7 Sept 2018

Neumann GA (2017) Mercury Laser Altimeter (MLA) Navigation Assessment (NAVASSMT) documents. https://pds-geosciences.wustl.edu/messenger/mess-e_v_h-mla-3_4-cdr_rdr-data-v2/messmla_2101/document/navassmt/navinfo.txt. Accessed 22 July 2020

Neumann GA, Rowlands DD, Lemoine FG, Smith DE, Zuber MT (2001) Crossover analysis of Mars Orbiter Laser Altimeter data. J Geophys Res Planets 106(E10):23753–23768. https://doi.org/10.1029/2000JE001381

Neumann GA, Cavanaugh JF, Coyle DB, McGarry J, Smith D, Sun X, Torrence M, Zagwodski TW, Zuber MT (2006) Laser ranging at interplanetary distances. In: Proceedings of the 15th international workshop on laser ranging, Canberra, Australia

Neumann GA, Perry ME, Mazarico E, Ernst CM, Zuber MT, Smith DE, Becker KJ, Gaskell RE, Head JW, Robinson MS, Solomon SC (2016) Mercury shape model from laser altimetry and planetary comparisons. In: Lunar and planetary science conference, vol 47, p 2087

Nolting W (2013) Grundkurs Theoretische Physik 4: Spezielle Relativitätstheorie, Thermodynamik. Springer, Berlin

Parro LM, Jimenezdiaz A, Mansilla F, Ruiz J (2017) Present-day heat flow model of Mars. Sci Rep 7(1):45629. https://doi.org/10.1038/srep45629

Perry ME, Neumann GA, Phillips RJ, Barnouin OS, Ernst CM, Kahan DS, Solomon SC, Zuber MT, Smith DE, Hauck SA, Peale SJ, Margot JL, Mazarico E, Johnson CL, Gaskell RW, Roberts JH, McNutt RL, Juergen O (2015) The low-degree shape of Mercury. Geophys Res Lett 42(17):6951–6958. https://doi.org/10.1002/2015GL065101

Robbins SJ, Hynek BM (2013) Utility of laser altimeter and stereoscopic terrain models: application to Martian craters. Planet Space Sci 86:57–65. https://doi.org/10.1016/j.pss.2013.06.019

Rowlands DD, Pavlis DE, Lemoine FG, Neumann GA, Luthcke SB (1999) The use of laser altimetry in the orbit and attitude determination of Mars Global Surveyor. Geophys Res Lett 26(9):1191–1194. https://doi.org/10.1029/1999GL900223

Shapiro II (1964) Fourth test of general relativity. Phys Rev Lett 13(26):789–791. https://doi.org/10.1103/PhysRevLett.13.789

Shutz BE, Urban TJ (2014) The GLAS algorithm theoretical basis document for laser footprint location (Geolocation) and surface profiles. Algorithm Theoretical Basis Documents (ATBD)

Smith DE, Zuber MT, Frey HV, Garvin JB, Head JW, Muhleman DO, Pettengill GH, Phillips RJ, Solomon SC, Zwally HJ, Banerdt WB, Duxbury TC, Golombek MP, Lemoine FG, Neumann GA, Rowlands DD, Aharonson O, Ford PG, Ivanov AB, Johnson CL, McGovern PJ, Abshire JB, Afzal RS, Sun X (2001a) Mars Orbiter Laser Altimeter: experiment summary after the first year of global mapping of mars. J Geophys Res Planets 106(E10):23689–23722. https://doi.org/10.1029/2000JE001364

Smith DE, Zuber MT, Neumann GA (2001b) Seasonal variations of snow depth on Mars. Science 294(5549):2141–2146. https://doi.org/10.1126/science.1066556

Smith DE, Neumann GA, Arvidson RE, Guinness EA, Slavney S (2003a) Mars Global Surveyor laser altimeter Mission Experiment Gridded Data Record (MEGDR). NASA Planetary Data System. Tech. rep., MGS-M-MOLA-5-MEGDR-L3-V1.0

Smith DE, Zuber MT, Neumann GA (2003b) Mars Orbiter Laser Altimeter (MOLA) Planetary Data Syatem (PDS) pedrds.cat. https://pds-geosciences.wustl.edu/mgs/mgs-m-mola-3-pedr-l1a-v1/mgsl_21xx/catalog/pedrds.cat. Accessed 7 Sept 2018

Smith DE, Zuber MT, Neumann GA, Mazarico E, Lemoine FG, Head JW III, Lucey PG, Aharonson O, Robinson MS, Sun X, Torrence MH, Barker MK, Oberst J, Duxbury TC, Mao D, Barnouin OS, Jha K, Rowlands DD, Goossens S, Baker D, Bauer S, Gläser P, Lemelin M, Rosenburg M, Sori MM, Whitten J, Mcclanahan T (2017) Summary of the results from the Lunar Orbiter Laser Altimeter after seven years in lunar orbit. Icarus 283:70–91. https://doi.org/10.1016/j.icarus.2016.06.006

Stark A, Oberst J, Preusker F, Peale SJ, Margot JL, Phillips RJ, Neumann GA, Smith DE, Zuber MT, Solomon SC (2015) First MESSENGER orbital observations of Mercury's librations. Geophys Res Lett 42(19):7881–7889. https://doi.org/10.1002/2015GL065152

Steinbrügge G, Stark A, Hussmann H, Sohl F, Oberst J (2015) Measuring tidal deformations by laser altimetry. A performance model for the Ganymede Laser Altimeter. Planet Space Sci 117:184–191. https://doi.org/10.1016/j.pss.2015.06.013

Steinbrügge G, Stark A, Hussmann H, Wickhusen K, Oberst J (2018) The performance of the BepiColombo Laser Altimeter (BELA) prior launch and prospects for mercury orbit operations. Planet Space Sci 159:84–92. https://doi.org/10.1016/j.pss.2018.04.017

Sun X, Neumann GA (2015) Calibration of the Mercury Laser Altimeter on the MESSENGER Spacecraft. IEEE Trans Geosci Remote Sens 53(5):2860–2874. https://doi.org/10.1109/TGRS.2014.2366080

Thomas N, Spohn T, Barriot JP, Benz W, Beutler G, Christensen U, Dehant V, Fallnich C, Giardini D, Groussin O, Gunderson K, Hauber E, Hilchenbach M, Iess L, Lamy P, Lara LM, Lognonné P, Lopez-Moreno JJ, Michaelis H, Oberst J, Resendes D, Reynaud JL, Rodrigo R, Sasaki S, Seiferlin K, Wieczorek M, Whitby J (2007) The BepiColombo Laser Altimeter (BELA): concept and baseline design. Planet Space Sci 55(10):1398–1413. https://doi.org/10.1016/j.pss.2007.03.003

Thomas N, Hussmann H, Lara LM (2019) The BepiColombo Laser Altimeter (BELA): a post-launch summary. CEAS Space J 11(4):371–380. https://doi.org/10.1007/s12567-019-00270-y

Turyshev SG, Farr W, Folkner WM, Girerd AR, Hemmati H, Murphy TW, Williams JG, Degnan JJ (2010) Advancing tests of relativistic

gravity via laser ranging to Phobos. Exp Astron 28(2–3):209–249. https://doi.org/10.1007/s10686-010-9199-9

Zhou H, Chen Y, Hyyppä J, Li S (2017) An overview of the laser ranging method of space laser altimeter. Infrar Phys Technol 86:147–158. https://doi.org/10.1016/j.infrared.2017.09.011

Zuber MT, Smith DE, Solomon SC, Muhleman DO, Head JW, Garvin JB, Abshire JB, Bufton JL (1992) The Mars Observer Laser Altimeter investigation. J Geophys Res Planets 97(E5):7781–7797. https://doi.org/10.1029/92JE00341

Zuber MT, Smith DE, Phillips RJ, Solomon SC, Neumann GA, Hauck SA, Peale SJ, Barnouin OS, Head JW, Johnson CL, Lemoine FG, Mazarico E, Sun X, Torrence MH, Freed AM, Klimczak C, Margot JL, Oberst J, Perry ME, McNutt RL Jr, Balcerski JA, Michel N, Talpe MJ, Yang D (2012) Topography of the northern hemisphere of Mercury from MESSENGER laser altimetry. Science 336(6078):217–220. https://doi.org/10.1126/science.1218805